# Effect of PVdF distribution on properties and performance of dry spray-coated graphite electrodes for lithium-ion batteries for electric vehicle applications

J. Alberto Barreras-Uruchurtu, Nicolas Besnard, Clément Paul, Lauréline Marchal, Samuel Devisme, Bernard Lestriez

**Title: Effect of PVdF distribution on properties and performance of dry spray-coated graphite electrodes for lithium-ion batteries for electric vehicle applications**

Author Names: J. Alberto Barreras-Uruchurtu[1,2,z], Nicolas Besnard[2], Clément Paul[3], Lauréline Marchal[4], Samuel Devisme[3], Bernard Lestriez[1,z]

Affiliation(s):
[1]Nantes Université, CNRS, Institut des Matériaux de Nantes Jean Rouxel, IMN, Nantes F-44000, France
[2]Ampere (Renault Group), Technocentre, 1 avenue du Golf, 78288 Guyancourt, France
[3]Arkema, Centre de recherche, développement, applications et technique de l'ouest (CERDATO) Serquigny, France
[4]Arkema, Centre de Recherche Rhône-Alpes (CRRA) Lyon, France
[z]Corresponding Author E-mail Address [bernard.lestriez@cnrs-imn.fr : jesus-alberto.barreras-uruchurtu@renault.com]

**Abstract Text**

In this work, we use electrostatic dry spray-coating to fabricate graphite/PVdF anodes. We compare the morphological, mechanical, electrical and electrochemical properties of electrodes fabricated with three different mixing times of dry electrode components. Quantitative and novel relationships between the PVdF distribution and the electrode properties are obtained. Our investigations suggest that our fabrication methods are viable alternatives for producing electrodes with comparable properties to those fabricated using traditional wet solvent-based methods. Overall, our work provides insights into new and promising methods for fabricating high-quality dry-sprayed electrodes (DSEs) with high mass loadings for use in a variety of electrochemical applications such as electric vehicles.

**Introduction Text**

Lithium-ion batteries (LIBs) have become the main energy storage technology for consumer electronics and electric vehicles (EVs). Conventional LIB electrodes are manufactured by coating solvent-based mixtures onto metallic current collectors. These mixtures typically consist of an electrochemically active material, a conductive carbon, a polymer binder, and a solvent that is used for binder dissolution. A widely employed binder/solvent combination in LIBs is polyvinylidene fluoride (PVdF) dissolved in N-methyl-2-pyrrolidone (NMP) for the cathode while for anodes, a sodium salt of carboxymethyl cellulose (CMC) and styrene-butadiene rubber (SBR), both dissolved in water is usually employed.[1]

Recently, there has been a growing interest in developing new electrode manufacturing processes that are more environmentally sustainable and economically viable[1–3]. The dry

battery manufacturing process involves fabricating electrodes without the use of solvents, directly depositing active materials onto current collectors, and eliminating the need for a drying step.[4] The growing and recent interest in these processes can be attributed to the numerous advantages they offer compared to traditional manufacturing methods. In the case of the cathode, eliminating the use of NMP, a hazardous solvent with significant energy costs associated with its evaporation, recovery, and recycling, accounts for almost 47% less energy consumption during the manufacturing process and around less than 15% of the total costs including manufacturing, capital, energy and material cost[3,5]. This approach is also relevant for the anode, where water is used as a solvent in the fabrication process. There are several types of dry battery manufacturing processes[6–10], and amongst them, polytetrafluoroethylene (PTFE) based processes like the Maxwell-process[11,12] are one of the most widely studied[13–15]. This process involves the dry blending, dry PTFE fibrillizing, dry compacting/calendaring, and bonding to the current collector. The high plasticity of PTFE allows forming fibers under shearing to connect electrode particles. However, there are challenges associated with PTFE in LIB anodes since it is known for its unstability at low potential,[16] contributing to capacity loss in the early stages of battery cycling[14,17]. PTFE production has also been singled out as having significant environmental impacts[18].

In this work, we will be focalizing in electrostatic dry spray-coating graphite anodes using PVdF as a binder. In this process, a high voltage is applied to a previously dry-mixed electrode powder, which then gets electrically charged, forming a cloud of charged particles. The charged particles are then accelerated towards the grounded current collector, where they form a uniform and continuous coating layer, which is then hot pressed to thermally activate the binder and control the coating thickness and density. This way, both cathodes ($LiCoO_2$,[4] $LiNi_{0.33}Mn_{0.33}Co_{0.33}O_2$[19], $LiNi_{0.5}Mn_{0.3}Co_{0.2}O_2$[19], $LiNi_{0.8}Mn_{0.1}Co_{0.1}O_2/LiMn_2O_4$[20]) and anodes ($Li_4Ti_5O_{12}$[7,21], graphite[20]) have been prepared, in most cases with PVdF binder[4,7,19–21]. In Schälicke et al.'s work on graphite-based electrodes, PVdF was judged to be an unsuitable binder for this process, the reason being however that the grade of PVdF used had too large particle sizes ($d_{50}$ of 85µm). This is why they obtained better results with a fluorinated ethylene propylene copolymer or a copolymer of tetrafluoro ethylene, hexafluoro propylene, and vinylidene fluoride ($d_{50}$ of 5µm). Some studies have shown that electrodes fabricated using this method can exhibit strong electrochemical and mechanical performances, approaching and even surpassing that of wet-processed electrodes, even for short mixing and hot pressing durations[4,22] and low binder content [23].

This change in the manufacturing process can affect the electrode characteristics such as homogeneity of distribution, porosity, adhesion, and cohesion between active material and carbon black (CB) conducting agent particles and the current collector, electrical properties, and therefore the battery performance[24–27]. The uniform mixing distribution of the binder and CB additive materials throughout the active material is crucial for manufacturing dry-processed LIB electrodes [23,28]. The degree of dry mixing was found to have a pronounced impact on the morphology and homogeneity of electrostatic screen printed $LiNi_{1/3}Co_{1/3}Mn_{1/3}O_2$/PVdF/CB (91:3:6) cathodes, which in turn affected their mechanical strength and electrochemical performance[28]. In this study by Yonaga et al., the electrode powder was mixed using a vertical high-shear mixer for 30 minutes at rotation speeds of 1,000, 3,000, and 10,000 rpm. The results showed that a coarse CB distribution, obtained at lower rotation speeds, resulted in lower performance due to insufficient contact between the CB phase and the $LiNi_{1/3}Co_{1/3}Mn_{1/3}O_2$ phase. However, a distribution that is too fine, observed at higher rotation speeds, led also to lower performance due to inadequate percolation of CB within the electrode. Wang et al. studied the effects of two dry powder mixing processes prior to electrostatic spray deposition of $LiNi_{0.8}Mn_{0.1}Co_{0.1}O_2/LiMn_2O_4$/PVdF/CB (48:48:2:2) electrodes.[20] The powders were mixed either using a high-speed planetary centrifugal mixer (4 cycles of 4 min with revolution speed of 880 rpm, rotation speed of 880 rpm) or a planetary ball mill (60 min at rotation speed of 300 rpm). Electrodes made using the first method had a dense CB/PVdF layer on the active material particles, limiting their contact area with the electrolyte, while electrodes made using the second one exhibited a porous structure, enabling more active material-electrolyte contact, thus lowering charge transfer resistance, improving ionic conductivity and rate performance. The mechanical peel strength of the electrodes made using high-speed planetary centrifugal mixer was however four times superior. However, rationalizing all these findings is challenging due to variations in the tools and conditions used to mix the electrode powders.

For our study, we prepared electrode powder mixtures consisting of 97 wt.% graphite and 3 wt.% PVdF through a dry-mixing process at room temperature, varying the mixing time. Then, these dry powders were subjected to a high-voltage electrostatic dry-spray process and applied onto a carbon-coated copper current collector. Afterwards, the electrodes were calendered at high temperature with a determined applied force. ***Figure 1*** depicts the different steps of fabrication and shows the resulting electrodes. Characterization of the electrodes included morphology assessment using SEM and EDS, as well as surface resistivity measurements. Mechanical properties were assessed through peel strength tests to measure electrode-current collector adhesion force and nanoindentation tests for hardness, elastic

modulus, and plasticity. Electrochemical evaluations were conducted using CR2032 half-cells with DSEs and reference wet-slurry electrodes (WSE). Our findings indicate that these fabrication techniques offer viable alternatives, yielding high-quality DSEs with short production time, good electrochemical and mechanical properties, against those produced through conventional wet-slurry based methods. Particular attention was paid to the analysis of the mixing quality in the electrode powders. The use of image analysis tools allowed us to quantify the fraction of binder distributed finely on the surface of the graphite particles from those forming agglomerates, allowing us to better understand and rationalize the influence of the distribution of the PVdF binder on the properties of these electrodes.

## Experimental

### Electrode fabrication

*Dry-sprayed electrodes (DSEs) fabrication*

97 wt.% graphite (GHDR 15-4, Imerys S.A.) and 3 wt.% PVdF (experimental grade, primary particle size 270 ± 26 nm, melt viscosity at 230 °C, 100 $s^{-1}$ is 23.5 – 29.5 kPoise, Arkema S.A.) anodes were fabricated by dry-mixing in a high intensity paddle mixer (Zeppelin Group) at room temperature. First, PVdF is sieved using a 355 µm pore size mesh. Then, PVdF is pre-mixed with graphite for 2 minutes at 800 rpm and then mixed at 1500 rpm for 1 minute (short-mixed electrode powder, indicated 1-SM), 3 minutes (moderate-mixed electrode powder, indicated 3-MM) and 15 minutes (long-mixed electrode powder, indicated 15-LM). The powder mixes are heated overnight at 100 °C under vacuum to limit humidity content. A high voltage (around 25 kV) is then applied to each electrode powder mixture using an electrostatic spray gun (Gema Switzerland GmbH), forming a cloud of particles that are applied directly onto a carbon-coated (1 µm of coating) 9 µm copper current collector (EnSafe®, Armor Battery Films, France). The coating, consisting of a submicron binder and conductive layer, improves the adhesion of the dry electrode to the current collector. The distance between the electrostatic spray gun and the current collector is 20 cm approximately. The electrode produced was then passed through a calendering machine (CA3 model, Sumet Technologies GmbH & Co. KG**)** at 160 °C temperature with an applied force of around 50 N $mm^{-1}$ at a rolling speed of 0.5 m of electrode per minute.

*Wet-slurry electrodes (WSEs) fabrication*

For comparison, reference wet-slurry electrodes (WSEs) were also fabricated using a slurry coating process. The electrode composition consisted of 94 wt.% graphite (GHDR 15-4, Imerys S.A.) and 3 wt.% CMC (BVH9, Ashland Bondwell), 1 wt.% SBR (BM 451B, Zeon) and 2% CB (C65, Imerys S.A). The WSEs were designed to have similar mass loading and porosity to the DSEs and were coated onto a 10 µm bare copper foil (*PI-KEM Ltd.*).

**Characterizations**

*Morphology characterization*

The surface and cross-section morphology of electrodes was investigated using a Scanning Electron Microscope (SEM) (JSM7600F, Jeol) coupled with Energy Dispersive X-ray Spectroscopy (EDS) from Bruker. Additionally, a cross-section ionic polisher (Jeol) was employed to prepare electrode samples before imaging.

*Electrical measurements*

Powder mixture resistivity*:* Powder mixture resistivity was assessed through impedance tests conducted using a Swagelok cell without a spring, using a hydraulic press (Syrio Dental Division) maintaining constant pressure throughout the testing process. The voltage amplitude (Va) was set at 50 mV, and measurements were taken within the frequency range of 10 mHz to 200 kHz.

Electrode surface conductivity*:* An automatic four-point probe (280I series, Four Dimensions Inc.) was used to perform surface resistivity measurements of the electrodes, including the current collector. We measured 49 points for each sample, and made necessary corrections for thickness variations.

*Mechanical measurements*

Nanoindentation*:* Tests to determine hardness (H) and elastic modulus (E) were performed using a nanoindentation tester (HIT 300, Anton Paar). Force applied was 0.1–75 mN, resulting in a penetration depth of approximately 10-15 µm for each sample. The measurements were conducted in ‘sinus mode’ (dynamic mechanical analysis), a frequency of 5 Hz and an amplitude of 7.5 mN (10% of the maximum force) was applied during the loading phase, at a constant strain load rate/load of 0.2 $s^{-1}$. A 60s pause at maximum force (creep step) is applied before unloading.

Peel strength*:* The peel strength was performed used an electromechanic test equipment (Criterion, MTS Systems®) with a 100 N module.

*Electrochemical measurements*

Coin cell format – Rate capability and long-term cycling: CR2032 type half-cells were assembled with DSEs and reference WSE (0.785 $cm^2$ disc). A lithium metal foil (0.38mm, 99.9%, Sigma-Aldrich) was used as counter electrode. One glass microfiber (Whatman CF/D) was used as separator and LP30 electrolyte (1.0 M lithium hexafluorophosphate ($LiPF_6$) in 1:1 volume of ethylene carbonate (EC) and dimethyl carbonate (DMC)). The cells were assembled in an argon-filled glove box using an automatic coin cell crimper (MTI Corporation). Testing was conducted from 0.005 V to 1.0 V vs. $Li/Li^+$ using a multi-channel battery testing system (BioLogic). The protocol included three lithiation/delithiation cycles under a constant-charge rate (CC) of 0.1C (1C corresponds to 360 mAh/g of graphite) followed by a constant-voltage (CV) with a current cutoff equal to ±0.05C at both the end of the lithiation and delithiation (0.00 5 and 1.0 V, respectively). Then, to evaluate the electrodes rate capability, a CCCV (constant-charge constant-voltage) lithiation (0.2C – 0.005 V with a current cutoff at 0.1C) followed by a CC delithiation, which included various current rates (0.2C, 0.5C, 1C, 1.5C, 2C, 5C, 10C, with three cycles for each rate). Finally, to assess the long-term cycling performance of the electrodes, lithiation and delithiation were carried out at a CC rate of 0.2C.

Pouch cell format – Long term cycling: Full-cells in pouch format were assembled in an argon-filled glove box using our DSEs and WSE as the anode. The composition of the WSE remained the same, but it is from a different series than the WSE used in the other tests. The electrode surfaces were 16 $cm^2$ for the anode and 14.44 $cm^2$ for the cathode. The mean N/P ratio was 1.1 ± 0.05. The cathode was prepared using a wet-slurry process and is composed of 97% $LiNi_{0.8}Mn_{0.1}Co_{0.1}O_2$, NMC 811 (Ningbo Ronbay New Energy Technology Co., Ltd.), 1.5% CB (C65, Imerys S.A), and 1.5% PVdF (Solef 5130, Solvay). The mean mass loading is 20.6 ± 0.3 mg $cm^{-2}$. The mean porosity is 28.3 ± 0.8 %. The electrolyte used was LP57 + 2% VC (1 M $LiPF_6$ in a mixture of EC and ethyl methyl carbonate (EMC) (3:7 by weight), with a 2 wt.% vinylene carbonate additive) with an NKK-TBL4620 cellulose separator (Nippon Kodoshi Corporation). The volume of electrolyte used was 500 µL. The formation process included two full cycles at a 0.1C rate, followed by degassing. To assess the long-term cycling performance of the electrodes, lithiation and delithiation were carried out at a constant charge (CC) rate of 0.2C over more than 150 cycles, within the voltage range of 2.7 to 4.2 V. The testing was conducted using a multi-channel battery testing system (Bio-Logic).

Tortuosity factor determination*:* Symmetrical coin cells were assembled using two electrodes of different areas (1.77 and 1.13 $cm^2$) with one polypropylene Celgard 2400 separator. An electrolyte of 12mM of tetrabutylammonium hexafluorophosphate ($TBAPF_6$) in a 1:1 in weigth dimetylcarbonate and diethylcarbonate mixture (DMC/DEC) was added to the cell. The cells were assembled in an argon-filled glove box using an automatic coin cell crimper (MTI Corporation). Potentiostatic electrochemical impedance spectroscopy (PEIS) was conducted on the coin cells on an electrochemical testing instrument (VMP, Bio-Logic), employing a voltage amplitude of 10mV and a frequency range of 1MHz to 0.1Hz. The average of three measurements was used in all our calculations.

*Post-cycling analysis*

CR2032 type half-cells were assembled using the protocol described in the rate capability and long-term cycling section, but using a larger electrode disc (1.76 $cm^2$) and an additional polypropylene monolayer separator (Celgard 2400) on the graphite electrode side to facilitate electrode recovery. After cycling, the cells were delithiated at a C/20 rate, then disassembled using an automatic coin cell crimper (MTI Corporation) and washed carefully with a few droplets of DMC and finally dried at 40 °C under vacuum for 2 hours. Electrode surface conductivity tests were performed (as described in Electrical measurements) as well as nanoindentation tests (as described in Mechanical measurements). Solid-State Magic-Angle Spinning Nuclear Magnetic Resonance (MAS-NMR) analysis were acquired on a Bruker 500 MHz Ultrashield spectrometer ($B_0$ = 11.8 T, Larmor frequencies $\nu_0(^7Li)$ = 194 MHz) to monitor the electrodes after the 3 formation cycles. The samples were prepared by recovering the electrodes inside an Argon-filled glovebox. The recovered powder samples were packed in 2.5 mm zirconia rotors inside an Argon-atmosphere glovebox. The spinning frequency was 25 kHz. The spectra for $^7Li$ NMR were acquired by employing a single pulse sequence with a recycle time of 60 s. The long recycle times or delays were used to ensure full relaxation and quantitative results. All MAS-NMR experiments were performed at room temperature.

## Results

### Electrode powder mixtures

SEM imaging has been employed to qualitatively assess the quality of electrode powder mixture at three different times, each corresponding to different mixing durations. Pristine graphite particles can be observed in ***Figure S1a-b***. Before the mixing process begins, PVdF primary particle of ~270 nm initially forms agglomerates of several micrometers (as seen in

***Figure S1c-d***), which gradually begin to disperse and break apart with an extended duration of mixing. As mixing time increases, these agglomerates continue to break down further, allowing the individual PVdF particles to coat an increasing portion of the graphite particles surface (***Figure 2a-i***). This phenomenon ultimately leads to a higher coverage of electrically conductive graphite particles by electrically insulating PVdF particles. Furthermore, the fraction of PVdF particles forming agglomerates decreases over time.

We conducted image analyses on SEM images using the ImageJ software, with examples presented in ***Figure S2***. We obtained mean values of fraction of graphite surface covered by PVdF particles ($\chi_{Gr,PVdF}$), of 0.23 ± 0.03 for 1-SM, 0.34 ± 0.06 for 3-MM and 0.45 ± 0.07 for 15-LM (see ***Table I***). In order to determine the maximum coverage rate of graphite particles by PVdF particles, we conducted an estimation of the total surface area generated by PVdF particles ($S_{PVdF}$). We assume each particle maintains a circular shape when covering graphite (as observed ***Figure S2***). Next, we calculated the total surface area of graphite particles ($S_{Gr}$), assuming a spherical shape. Using a PVdF particle size of 270 nm (determined as the mean value through SEM image analysis) and a graphite particle size of 16.1 µm (De Brouckere [D 4,3] or volume-weighted mean diameter obtained by granulometry), we found that, at a PVdF 3 wt.%, the maximum coverage rate ($CR_{max}$) is 54.9% (**Equations S1-S3**). This means that if all our PVdF particles were covering the graphite, the maximum percentage of the total graphite surface they can cover is only 54.9%. This calculation assumes all PVdF adheres to graphite particles, i.e. are completely deagglomerated and forming a monolayer. At the end, we could determine the fraction of PVdF present on the surface of the graphite particles ($\chi_{PVdF,Gr}$), and the fraction that is still in the form of agglomerates ($\chi_{PVdF,agglo}$), for the different mixing times (see ***Table I***).

Then, by performing complimentary SEM image analysis we determined the mean agglomerate size for each mixture (examples found in ***Figure S3***). It can be observed that the mean agglomerate diameter ($D_{agglo}$) decreases with mixing time, ***Table I***. Additionally, we estimated the mean number of PVdF particles constituting one agglomerate ($N_{PVdF\ per\ agglo}$) for each mixing time. This calculation assumes random close-packing (RCP) of spheres and employs the highest achievable average density for the arrangement of monodisperse sphere ($\Phi_{RCP}$), approximately 0.64[29]. We proceeded to estimate the number of agglomerates ($N_{agglo}$) present in each mixture per gram of electrode powder mixture (refer to ***Table I***). Our analysis revealed that 3-MM mixture, characterized by a moderate mixing time, maximizes the number of agglomerates in our powder mixtures, with these agglomerates exhibiting an intermediate size. The 1-SM and 15-LM samples present only approximately half of the agglomerates

observed in the 3-MM mixture. ***Table I*** also provides the fraction of PVdF either distributed at the surface of graphite particles ($\chi_{PVdF,Gr}$) or in the form of agglomerates ($\chi_{PVdF,agglo}$), according to these calculations. The standard deviation in the number of PVdF agglomerates are notably high, approximately 42%, 29%, and 17% of the average. This is likely due to both the contribution of the standard deviation in the fraction of graphite surface covered by PVdF and the standard deviation of agglomerate sizes, which are not uniform across the powder mixtures. Additionally, the low number of observable agglomerates in the SEM images, with only around ten images analyzed per sample, contributes to this variability. While increasing the number of acquisitions could provide a more accurate determination of the number of agglomerates, it is likely that the standard deviation of PVdF agglomerates remains high due to the intrinsic variability of agglomerate sizes.

***Figure 3a*** shows an experimental set-up we used to determine electrical resistivity at different pressures. We filled a 12.7 cm diameter Swagelok cell with the electrode powder mixture (0.5 g) and we applied a constant pressure between 0 and 77 MPa. We acquired three impedance spectra (EIS) for each pressure, and the ohmic resistance of the powder confined between the two pistons is determined by reading its value at the point where the impedance spectrum intersects the real axis on the Nyquist plots (Im[Z] vs Re[Z]). ***Figure 3b***, demonstrates the impact of applied pressure on the sample density. Logically, the larger the pressure applied the greater the density for all samples, but not all powder mixtures compact in the same manner, due to rheological properties like cohesion strength. This variability will be reported in a forthcoming paper. When the sample mass is kept constant at 0.50 g, we observe that 1-SM achieves greater compaction compared to the other two mixtures. For example, for an applied pressure of 50 MPa, while density in g $cm^{-3}$ is around 1.64 for 3-MM and 1.61 for 15-LM, this value is 1.97 for 1-SM, which is 20% greater. In a following experiment with a higher sample mass (0.75 g) at the same applied pressure, 1-SM's compaction level decreased, aligning with values similar to 3-MM and 15-LM. This variability in compaction behavior is likely due to different powder cohesion strength values, which will be reported in a forthcoming paper. We opted to compare resistivity values at constant density because it offers a more precise analysis of the influence of binder agglomerates and graphite particles distribution in the mixtures than using constant pressure. In ***Figure 3c***, we observe that 1-SM consistently exhibits the lowest resistivity at all density values, indicating the best electrical conductivity, while 15-LM has the highest electric resistivity with the highest sensibility to pressure changes. 3-MM shows close but still higher values than 1-SM. It shows that ohmic resistance of these powder mixtures rise

with the prolonged mixing time. This trend is rationalized in **Figure 3d**, where we plotted the mean powder electrical resistivity (between 1.6 and 1.77 g $cm^{-3}$), vs the fraction of PVdF particles that are covering the graphite. It shows that ohmic resistance of these powder mixtures rise with the prolonged mixing time, as the electronic pathways within the composite are increasingly blocked by the insulating binder particles being more localized at contacts between graphite particles.[30,31] These values are furthermore in the same order of magnitude as other values reported in the literature (214 mΩ·cm for a 97 wt.% graphite electrode with 1 wt.% CMC, 1 wt.% SBR and 1 wt.% conductive carbon).[32]

## Consolidated electrode

*Morphology and microstructure*

Technical information about the electrodes is available in ***Table II***. To evaluate the impact of the consolidated electrodes structure on mechanical and electrochemical properties, we conducted an analysis as shown in ***Figure 4.*** These SEM images feature cross-sections and fluorine EDS mapping for PVdF-based DSEs and sodium for the reference CMC-based WSE. These SEM images provide a comprehensive view of how varying mixing conditions influence electrode binder distribution, using fluorine as a "marker" for PVdF distribution and sodium for CMC distribution. In ***Figure. 4a-b*** we observe 1-DSE, exhibiting a poor homogeneity of PVdF, with a bigger concentration in the middle of the electrode and a poorer concentration close to the current collector and close to the electrode surface. The PVdF rich area in these electrodes are due to the PVdF agglomerates in the electrode powders. In contrast, ***Figure 4d-e***, representing 3-DSE, displays a marked improvement in homogeneity, although some areas still exhibit higher fluorine concentration, also indicative of agglomerates observed in the powder mixture (see ***Figure. 2***). In **Figure *4g-h***, we see long mixing times result in even better homogeneity within the electrodes, with nearly no binder agglomerates present in the mixture, as expected. These morphologies are consistent with that of the powders. Finally, in ***Figure 4j-k***, which show reference WSE, displays good CMC binder distribution as well.

***Figure 4*** also displays four SEM images, magnified between 2.5kX and 4.0kX, focusing on graphite particles and the binder structure within the electrode. A distinct contrast is evident between the morphologies of the three DSEs (***Figure 4c, f, and i***) and the WSE (***Figure 4l***), directly attributable to the fabrication process, and likely affecting the functionality of the electrodes. In DSEs, PVdF form ligaments, which are binding graphite particles thereby enhancing mechanical stability without fully encapsulating the particles in binder material. On

the contrary, WSEs rely on a veil-like film for mechanical support. While this film ensures robustness, it introduces a potential trade-off; being a binder film, it may elevate electrical resistivity due to its inherent insulating nature. There is a nuanced interchange between mechanical stability and electrical conductivity in WSE that we do not necessarily observe in DSEs, because of the different mechanism of binder distribution. Additional SEM images of the cross section of the electrodes are available in ***Figure S4***.

*Electrical properties*

We determined the sheet resistivity of the DSE using four-point probe measurements. For more clarity, we represented resistivity in mΩ cm (as shown in ***Figure 5a***). Electrode 1-DSE, with a resistivity of 0.069 ± 0.0024 mΩ cm, showcases the lowest resistivity amongst the DSEs. Comparatively, electrode 3-DSE presents a higher resistivity value than 1-DSE, which represents around 1.5 times the value of its resistivity (0.103 ± 0.0083 mΩ cm). 15-DSE exhibits the highest resistivity amongst the DSEs, with resistivity 0.418 ± 0.015 mΩ cm. This is also coherent with the fraction of graphite surface covered by PVdF in the powder mixtures (see ***Figure 5b***). The WSE exhibit a very large resistivity (3.41 ± 0.035 mΩ cm, which is 50 times higher than 1-DSE). It should be noted that the binder content is not the same (4 wt.% for WSE and 3 wt.% for the DSE), neither the CB one (2 wt.% for WSE and 0 wt.% for the DSE), which certainly has an impact on these values. The current collector is not the same either (DSE employs carbon coated copper as current collector and WSE just copper). DSEs ohmic resistivity values exhibit a consistent trend with those observed in the powder mixture (see ***Figure 3d***) but the values of resistivity are significantly lower. This can be due to differences in the experimental geometry (2- vs. 4-probe setups). The 2-probe method measures resistivity by applying current and measuring voltage through the same two probes, which includes contact resistance and can affect accuracy. In contrast, the 4-probe method uses separate probes for current supply and voltage measurement, eliminating contact resistance and providing more precise results[33]. In addition, the setup used for the 2-probe measurements means that the current lines only cross the sample and the interfaces between the sample and the electrodes. In 4-probes measurements this is also the case, but part of the current lines pass through the current collector due to its higher conductivity than that of the electrode. Thus the resistivity value measured in 4-probes is generally lower than that measured in 2-probes.[34]

*Mechanical properties*

Nanoindentations measurements were done on the surface of the electrodes. ***Table III*** gathers the values of the hardness (H), elastic modulus (E), the elastic and plastic works ($W_{elast}$ and $W_{plast}$), the total work ($W_{total}$, the sum of elastic and plastic work), as well a ratio of plastic work to total indentation work applied during loading ($\eta_{plastic}$). The way that these values are obtained is detailed in the Supporting Information (***Figures S5-S7***). Examples of indentation curves are shown **Figure S5**. The total indentation work is the mechanical energy used to perform indentation, including the creep step. The plastic work represents the part of this mechanical energy which is dissipated, due to irreversible displacement of particles relative to each other and collapse of porosities, as-well-as permanent deformation of the binder. The elastic work represents the mechanical energy which is recovered during unloading and is related to the reversible deformation of the sample.

The differences observed in indentation values amongst the DSEs could potentially be attributed to the binder distribution. Values for H, E, $W_{total}$, $W_{elast}$ and $W_{plast}$ are plotted in ***Figure 6a-b*** as a function of the fraction of graphite surface covered by PVdF. A more thorough distribution of PVdF, achieved through longer mixing times, results in a greater fraction of PVdF particles covering graphite (see ***Figure. 2***). This leads to a reduction in the number of hard contacts between the graphite particles, potentially explaining the initial high values of H and E of 1-DSE. Indeed, the PVdF phase, due to its lower hardness (ball indentation hardness reported in the literature between 62 and 110 MPa[35]) than graphite (reported between 210 to 426 MPa[36]), likely act as 'cushions,' creating “softer” contacts between graphite particles. It is worth noting that there is generally a greater standard deviation observed in the values for 1-DSE, especially for hardness, which again indicates heterogeneity in binder distribution, as suggested by previous findings during cross-sectional analysis (see ***Figure 4***). Furthermore, ***Figure 6b*** shows that the $W_{total}$ and $W_{plastic}$ both tend to increase with the coverage rate of the graphite particles by PVdF, which is consistent with the results presented in ***Figure 6a***. The PVdF phase which covers the graphite particles creates more plastic and sliding contacts between them.[37,38]

In indentation tests, the electrodes are stressed in compression mode. To continue with characterizing mechanical properties of the electrodes, we performed 180° peel tests on our DSEs. We observe in ***Figure 6c***, that amongst the different mixing durations, 3-DSE exhibited the highest peel strength of 47.0 ± 3.7 N/m. In contrast, 1-DSE resulted in a slightly lower peel strength of 36.3 ± 6.4 N/m, whereas 15-DSE showed a substantial reduction in peel strength to

$10.7 \pm 2.1$[37] N/m. WSE's peel strength was determined using a different equipment in other laboratory facility and the value obtained was 79 N/m, with a cohesive failure. In peel tests, when observing the delamination interface, the interpretation of the values depends on the relative strength between the adhesion of the electrode to the current collector and interparticle cohesion. If the adhesion of the electrode to the current collector is weak and the electrode cohesion is high, the tape can completely remove the electrode. However, if the adhesion strength of the electrode is greater than the cohesion strength, the tape will selectively remove a part of the electrode from the foil.[39,40] In ***Figure S8***, we observe the delamination interface for all the electrodes, which provides information about possible failure mechanisms. The closest to an adhesive failure is observed in the case of 3-DSE. We observe a mixture of cohesive and adhesive failure for 1-DSE and 15-DSE. In ***Figure 6d***, we propose a correlation between the peel strength and the number of agglomerates present in the electrode powder mixtures. It suggests the peel strength increases with the number of PVdF agglomerates, from 15-DSE to 1-DSE and then to 3-DSE. We hypothesize indeed that the enhanced cohesion is a result of the presence of PVdF agglomerates (present in a greater number in both 1-DSE and 3-DSE and decaying in 15-DSE). We can in fact argue that the PVdF particles which are located at the position of the contacts between the graphite particles, and which have been laminated between the latter following the hot calendering of the electrodes, offer only very low resistance when the electrode being torn from the current collector. While the masses of PVdF resulting from the melting of the agglomerates offer very high resistance, because significant plastic dissipation can occur in their large volume. Indeed, the energy per unit area to separate two surfaces covered by a polymer can be quantified and is roughly given by:

$$W_{sep} = \sigma_y \times h_f \quad (1)$$

where $\sigma_y$ is the binder tensile stress at which a plastic zone can form, and $h_f$ is its maximum width of it [41,42]. The latter is very thin for PVdF patches at contact points between graphite particles, and very big for PVdF agglomerates. However, the standard deviation in the number of PVdF agglomerates is too large to definitively affirm this trend, leaving it as a proposition for interpretation. These different mechanical measurements nevertheless reflect the subtle influence of the distribution of the polymer binder on the mechanical properties of the electrode. In compression (nanoindentation, calendering), it is clearly the binder distributed homogeneously on the surface of the particles and located at the contact points between them which dictates the properties, while in traction (peeling) these would be controlled by the binder

distributed discretely in the form of agglomerates. In practice the mechanical integrity of all these electrodes was sufficiently good for conducting assembling electrochemical cells.

*Electrochemical properties*

In ***Table II***, we observe the mass loading of our electrodes. Porosity determination equation can be found in **Supplementary Information, *Eq. S10-S12***. Non-intercalating or blocking-electrolyte method developed by Landesfeind et al.[43] was used for tortuosity factor ($\tau$) determination for the DSEs and the WSE. By simplifying the transmission-line model (TLM) it is possible to determine the tortuosity factor based on the ionic resistance $R_{ion}$, the total effective area of the electrode A (1.13 $cm^2$), the intrinsic ionic conductivity of the electrolyte $\kappa$ (0.48 $mS \cdot cm^{-1}$), the electrode porosity $\epsilon$, and the thickness of the electrodes d.

$$\tau = (R_{ion}\, A\, \kappa\, \epsilon)/d \quad (2)$$

We conducted PEIS on our electrodes, and we obtained the Nyquist plots as shown in ***Figure S9***. By analyzing these Nyquist plots, we can approximate the values of $R_{ion}$ and $\kappa$. Further details on this analysis can be found in the Supplementary Information (***Figure S10***). ***Table IV*** illustrates that the WSE exhibits a notably higher tortuosity factor compared to the DSEs, exceeding double that of both 1-DSE and 15-DSE. One potential explanation for this discrepancy is the elevated binder content in WSE (4 wt.% as opposed to 3 wt.%) which is highlighted in Landesfeind et al's work[44]. Additionally, the use of the CMC/SBR binder system in WSE, as mentionned in the same study, could potentially result in significantly higher apparent tortuosity values when compared to other binders including several types of PVdF. When comparing the DSEs, it appears that the tortuosity factor could also be correlated to the total number of agglomerates per g of electrode powder mixture (see ***Table IV***). An increase in the tortuosity factor with the addition of PVdF binder and CB has been previously observed for graphite anodes[44,45]. In our case, even though we are maintaining a constant PVdF rate, we could assume that it is the PVdF agglomerates that hinder diffusion. The mechanism being the swelling of PVdF by the electrolyte solvents (EC/DMC), which could form highly viscous microgels that can slow down diffusion[46]. This could explain the highest tortuosity factor observed for 3-DSE, where the number of PVdF agglomerates is maximized. Zacharias et al.[45], report tortuosity values twice as high as ours for graphite electrodes, but they use platelet-shaped graphite. In contrast, studies using spherical graphite find values between 2.7 and 4.3 for graphite electrodes with 4-6 wt.% PVdF, aligning closer with our own observations[44,47]. The study by Zacharias et al.[45] also demonstrates that modest variations in porosity, such as those

observed in our case, cannot account for an increase of more than 0.6 in tortuosity. However, the lower porosity of 3-DSE could also be at the origin of its higher tortuosity value.

***Figure S11*** shows first cycle charge-discharge curves. The voltage-capacity profile exhibits a characteristic pattern typically observed for graphite anodes. Coulombic efficiency of the first cycle is 92.1 ± 0.4% for 1-DSE, 91.8 ± 0.1% for 3-DSE, 92.4 ± 0.1% for 15-DSE, and 92.3 ±0.1% for WSE. These values are close with the reported value of 93% observed in graphite electrodes using PVdF as a binder, as documented in other studies.[48] In ***Figure 7a***, we observe a comparative analysis of representative electrodes under CC charge (delithiation) current rates ranging from 0.1C to 10C (mean capacity retention values of the half-cell series can be found in **Figure S12a-b)**. Each time, a CCCV lithiation (0.2C – 0.005V with a current cutoff at 0.1C) was systematically performed. At low charge current rates (0.1C to 0.5C) all electrodes retain over 98% of their initial discharge capacity after the first formation cycle. At 1C, the reference WSE retains approximately 89% of its initial discharge capacity, while the three DSEs retain around 98%. As the current rate increases to 1.5C, the reference WSE retains roughly 62% of its initial discharge capacity, while the short and moderate-mixed DSE retain approximately 94%, demonstrating their better retention potential even at higher rates. This is where we start seeing the capacity retention for the long-mixed 15-DSE electrode drop at 86%. At 2C, the short and moderate-mixed DSE retains between 76 and 79% of their capacity, while the 15-DSE capacity retention decreases to 46%. However, as the current rates escalate to 5C and 10C, both the WSE and DSEs experience substantial capacity drops. As the current rate is reduced back to 0.1C, all four electrodes exhibit a recovery in discharge current rate of over 98%. In ***Figure S13a-d***, we visualize the voltage profiles for each of the electrodes at three C-rates: 0.5C, 1C and 2C. There is a great contrast between the polarizations of the electrodes and the capacity retention during charge and discharge. It becomes clear that DSEs, particularly the short and moderate-mixed DSEs, consistently outperform the reference WSE in terms of discharge capacity retention at high current rate.

Numerous works have shown that the performance at high current rate, in delithiation as in lithiation, of high capacity graphite electrodes (over 3 $mAh \cdot cm^{-2}$) are dependent on the limitations imposed on the diffusion of the lithium salt across the electrode by the morphology of the latter.[32,49–51] These limitations are aggravated and performance reduced with increasing thickness and decreasing porosity of the electrode. As can be seen in ***Table II***, electrodes with similar porosities were selected for electrochemical testing. The comparison between 15-DSE and the other electrodes is however biased because this electrode has a higher active mass

loading and therefore higher thickness, which may result in additional charge transport limitations that could explain its lower rate performance. Furthermore, in the case of large graphite particles (> 10 µm), works showed an improvement in performance at high rate if CB is added. The latter, by multiplying the contacts between the large graphite particles, reduces the resistance to the charge transfer reaction (insertion/deinsertion of lithium with simultaneous injection/extraction of electron).[49,52] It could therefore be that the larger coverage of the graphite particles by the PVdF binder in 15-DSE penalizes the charge transfer reaction by minimizing electronic transfers between the graphite particles. In addition, the charge transfer reaction could also be penalized in this electrode by the stronger coverage of the graphite particles by the PVdF restricting the liquid electrolyte access to the surface of graphite.[53]

Tortuosity plays a crucial role in shaping the mass and charge transport dynamics within electrodes, impacting key parameters like effective ion conductivity and diffusivity in the electrolyte phase, and the maximum charge/discharge rate of batteries. Electrodes characterized by low tortuosity are favored, as they have the potential to improve energy storage, enhance charge storage kinetics, and facilitate ion transport.[44,54,55] This is particularly beneficial in the case of thick electrodes with high mass loading.[56] For the DSEs, we observe that power performance is not primarily explained by differences in tortuosity. Even though the 3-DSE exhibits slightly higher tortuosity, this does not penalize its power delivery. The poor performance of 15-DSE cannot be attributed to high tortuosity; rather, it is, as previously mentioned, the charge transfer reaction that is penalizing due to poor accessibility of ions and electrons caused by excessive graphite coverage by PVdF. We have demonstrated that the tortuosity factor for WSE is double that of the DSEs, which very likely explains its poorer rate performance. Its higher binder content and the use of a CMC/SBR binder system, as mentioned earlier, contribute to increased tortuosity compared to DSEs.

After conducting rate capability tests, we proceeded with long-term cycling tests on the same half-cells (***Figure 7b***). Representative coin cells with the closest values of mass loading and porosity were chosen to facilitate the comparison. Mean capacity retention values of the half-cells series can be found in **Figure S12c-d**. The capacity retention at the 100$^{th}$ cycle is 89.1% for 1-DSE, 86.7% for 3-DSE and 52.9% for 15-DSE whereas this value is only 77.1% for WSE. 1-DSE and 3-DSE exhibit higher capacity retention, suggesting a more robust long-term cycling performance compared to 15-DSE. The lower capacity retention of 15-DSE may be associated with its higher mass loading (see ***Table II***), along with poorer peel strength, and higher electrode resistivity, contributing to a potential reduction in durability. Similarly, WSE displays lower long-term cycling than 1- and 3-DSE, which could be linked to its elevated

electrical resistivity. Indeed, various works show a reduction in the electronic conductivity of the electrodes during cycling, and this more particularly in the case of graphite electrodes due to the variation in volume of the active material particles which generates tensile stresses within the electrode. These lead to a loss of electrical contacts and then to a loss of active matter [57,58].

In order to assess whether our electrodes would perform under conditions closer to the EV application, we fabricated full-cells in pouch format with DSEs and the reference WSE as anodes and a wet-slurry processed NMC 811 cathode. Long-term cycling (over 150 cycles at 0.2C rate is shown in ***Figure 7c***. Unfortunately, 1-DSE cycling was compromised by an accidental breakage of the electrode's tab during cycling, which interrupted the cycling. Before this incident, at the 70th cycle, 1-DSE, 3-DSE, and 15-DSE had capacities of 179.2, 188.2, and 173.4 mAh $g^{-1}$, with corresponding capacity retentions of 93.2%, 95.6%, and 88.8%. For comparison, the WSE is 190.3 mAh $g^{-1}$ or 96.9% capacity retention. At the 70th cycle, both 1-DSE and 3-DSE exhibited very good capacity retention, with 15-DSE showing the worst performance, which corresponds to the observations from the coin cell format half-cell testing.

After 150 cycles, the capacity retention values are 179.1 mAh $g^{-1}$ for 3-DSE-a and 135.9 mAh $g^{-1}$ for 15-DSE-a, corresponding to 91.0% and 69.6%, respectively. The WSE's capacity retention is 186.7 mAh $g^{-1}$, which represents 95.1%. Notably, 3-DSE-a maintained over 90% capacity retention after 150 cycles, which is a very promising result. The WSE performed well; it is important to note that the sample used for this test was further optimized and differed from the WSE used in the other tests in this article, although the composition remained the same. The poor performance of 15-DSE-a after 150 cycles is probably due to its inferior mechanical properties and elevated electrical resistivity.

***Figure S14*** shows the capacity profiles for the half-cell anodes at three moments of the experiment ($30^{th}$, $50^{th}$ and $80^{th}$ cycles, all performed at 0.2C). It reveals an increase of the cell polarization upon cycling. In ***Figure S15a-d***, the incremental capacity (dQ/dV = f(V)) profiles are observed for the $5^{th}$ cycle (solid lines) and for the $80^{th}$ cycle (dashed lines), both cycles being performed at 0.2C. Each of the lithiation (1-3) and delithiation (4-6) peaks have been numbered. These correspond to the successive stages of lithium intercalation and deintercalation in graphite ($Li_{0.22}C_6$-$Li_{0.34}C_6$, $Li_{0.5}C_6$, $LiC_6$).[59] We observe a clear shift of the peaks position that confirms the polarization of the cell. In ***Figure 8a-b***, we plotted the peaks position in five different cycles (5th, 30th, 50th, 60th and 80th) in order to visualize the polarization more clearly. The mean polarization increase between the $5^{th}$ and the $80^{th}$ cycle can be expressed as the average displacement ($\Delta V_{delith}$ - $\Delta V_{lith}$) of each (de)lithiation peaks. It is 56.9 mV for 1-DSE, 63.6 mV for 3-DSE, 78.3 mV for 15-DSE and 43.3 mV for WSE. A consistent trend is

observed for both lithiation and delithiation peaks, with 15-DSE exhibiting the greatest polarization, followed by 3-DSE and then 1-DSE. Notably, WSE shows a lower degree of polarization compared to the DSEs, indicating potentially reduced electrical degradation during cycling despite its inferior electrode performance, suggesting a different fading mechanism.

*Post-cycling analysis*

Supplementary half-cells were assembled for conducting post-cycling study of the ageing mechanisms. The DSEs underwent complete delithiation at a C/20 rate at two stages of cycling (after 3 and 75 cycles). One series was used for $^{7}$Li MAS-NMR analyses. Following the opening of the cells, electrodes were carefully washed with DMC, dried at 45 °C for 2 hours under vacuum and separated from the current collector. The dried electrode powder was then transferred into an NMR rotor in the glove box. The $^{7}$Li MAS-NMR spectra obtained appear in ***Figure S15.*** Broad peaks are observed at around 0 ppm for each of the electrodes. They typically correspond to lithium inorganic species such as lithium carbonate ($Li_2CO_3$), lithium hydroxide (LiOH) and lithium oxide ($Li_2O$) along with other lithiated organic species originating from solvent decomposition products, all present in the Solid Electrolyte Interphase (SEI).[60] Importantly, the intensity of these broad peaks is rather similar for all DSEs, suggesting that the amount of SEI is the same, and therefore independent of the PVdF distribution at the graphite surface. We expected that this would influence the quantity of SEI formed since the quantity of interface between the graphite and the electrolyte, which is the site of the electrolyte reduction, varies between the different DSEs.

Additional supplementary half-cells were assembled to conduct post-cycling electrical and mechanical properties measurements. The cyclability curves for these cells are provided in ***Figure S17***. It can be observed that the hierarchy within this series is similar to that of the first one, with 3-DSE and 1-DSE exhibiting much better capacity retention than 15-DSE. However, overall, this series performed less effectively than the first one. For instance, 3-DSE only shows a capacity retention of 70% compared to more than 90% in the first series. This difference may be attributed to the addition of a polypropylene separator and/or an aged electrolyte. Nevertheless, batteries were disassembled after 75 cycles and electrodes were rinsed with DMC and dried in the glove box. Electrode thickness increased by 12.5% for 1-DSE, 16.4% for 3-DSE and 18.5% for 15-DSE. A prior study on graphite and PVdF anodes, reported a 9% irreversible expansion during lithiation in the first cycle, leading to increased irreversible dilation with further cycling[61]. Another study reported 8 to 16% irreversible expansion at the

first charge depending on the crystallinity of the PVdF binder, a lower crystallinity resulting in higher irreversible dilation[62]. Higher PVdF crystallinity leads to stronger electrode cohesion[63].

The resulting electrical resistivity measurements are presented in ***Figure 9***. Despite the initial divergence in resistivity values in pristine electrodes, after cycling all three DSEs exhibit values of a similar magnitude (between 284 mΩ-cm for 15-DSE and 392 mΩ-cm for 3-DSE), all mean values being within error bars. We observe that there is an important increase of resistivity (× 300 to 5000) for all electrodes after cycling, in agreement with previous works[49,58]. Indeed, Pouraghajan et al. observed a decrease of conductivity and an increase of the contact resistance with the current collector with cycling for water-soluble-binder graphite electrodes, associated with their mechanical degradation, the volume changes in the electrode potentially resulting in loss of contacts. Furthermore, Grillet et al. found cyclic mechanical stresses cause significant degradation in the PVdF/CB films electrical conductivity. In the case of the WSE, the electrical resistivity values are approximately three times higher than those of the DSEs (968 mΩ-cm).

Results of nanoindentation measurements on cycled electrodes are given in ***Table III*** together with the relative variations for all parameters relative to pristine electrodes. An increase in hardness ($H_c$) and elastic modulus ($E_c$) can be noted, indicating an increase in the rigidity of the electrodes. The largest increase is observed for 15-DSE, whose stiffness and modulus even became higher than those of 1-DSE and 3-DSE, while they were lower for the pristine electrodes. The elastic work ($W_{elast}$) decreases in all cases while the plastic work ($W_{plast}$) increases for 1-DSE and 3-DES, but decreases for 15-DSE. These evolutions may reflect greater brittleness (more crumbly nature) of cycled electrodes, in particular for 15-DSE. This last electrode also shows a greater dispersion of Hc and Ec values which could also testify to the disintegration of this electrode, in agreement with its lower cyclability. Noteworthy, Wendt et al. also observed as here (see ***Table III***) an increase of the ratio of plastic work to total work ($\eta_{plast}$) upon cycling for PVdF-based cathodes,[64] attributed to weaker adhesion strength between particle/particle and particle/current collector due to delamination of PVdF domains under the combined effect of (i) repeated mechanical stresses from the expansion and compression of graphite particles during the reversible lithium insertion and (ii) the swelling of PVdF by electrolyte solvent.

Finally, for the DSEs, we highlight in ***Figure 10a*** the correlations between the increase in the graphite surface coverage by PVdF and the increase in their polarization during cycling on one hand and the decrease of the delithiation capacity at the 2C rate. In ***Figure 10b-c***, the

capacity retention at the 100$^{th}$ cycle is plotted as a function of the peel strength ~~and as a function of the number of PVdF agglomerates per g of electrode powder mixture~~. Indeed, the cycling conditions in CCCV are such that the increase in polarization has little effect on the capacity retention of the electrodes. The loss of capacity during cycling can therefore be associated with the mechanical disconnection of the active mass, following its volume variations and the expansion of the electrodes. Improving the cohesion of the electrodes, as measured by their peeling force, logically minimizes this phenomenon. The expansion of the electrodes naturally impacts the quality of electronic percolation. This degradation will be less pronounced if the initial quality is higher, thus the correlation between capacity retention and peel strength.

**Conclusions**

Using the electrostatic dry spray-coating method, a dry, solvent-free process, we were able to manufacture graphite/PVdF anodes with loadings typical of electric vehicle applications. These electrodes present electrical and mechanical properties, as well as electrochemical performance comparable to those of electrodes obtained using the state-of-the-art wet process, suggesting that this new process is a viable alternative to the latter.

The present work shows that the mixing step of graphite and PVdF powders is critical for all properties and electrochemical performance. Unlike the wet process, this step is very quick, only a few minutes. Contrary to what is commonly believed, the best distribution homogeneity does not guarantee the best performance. The distribution of PVdF is characterized by the presence of nanometric primary particles on the graphite surface and by micrometric agglomerates between the graphite particles. We quantified these two fractions and established, for the first time, quantitative relationships between the coverage rate of graphite particles by PVdF, the quantity of PVdF agglomerates, and the mechanical and electrical properties of the electrodes. The hardness, elasticity, and plasticity of the electrodes in compression, as well as the electrical resistivity are governed by the coverage rate of the graphite by the PVdF. Peel strength is governed by the quantity of PVdF agglomerates. The best electrochemical cyclability is obtained with electrodes whose powders have been mixed for a short time (5 minutes in total) and which have the best peel strength. With a longer mixing time (17 minutes), the quantity of agglomerates decreases as well as cyclability and peel strength. With a mixing time that is too short (3 minutes), the quantity of agglomerates, cyclability, and peel strength are high, but less good reproducibility of behavior is observed. Post-mortem analyzes show usual degradation phenomena for graphite/PVdF electrodes. The loss of cyclability is attributable to mechanical degradation of the electrodes during cycling. The presence of PVdF

agglomerates promotes better cohesion and therefore better resistance to variations in graphite volume. On another hand, the rate performance in discharge appears dictated by the coverage rate of the graphite surface by PVdF. A higher coverage resulting in poorer rate performance.

The grade of PVdF used as well as the conditions of implementation and in particular the temperature and duration of the heat treatment are factors which significantly affect the crystallinity of this binder. A direction of research for the optimization of this new process will therefore involve the selection or optimization of an ad hoc PVdF grade and hot calendering conditions. PVdF is overall a convenient and effective binder for this process, providing good mechanical stability and electrochemical performance to the electrodes. PVdF is overall a convenient and effective binder for this process, providing good mechanical stability and electrochemical performance to the electrodes. However increasing concerns have raised regarding per and polyfluoroalkyl substances (PFAS), persistent substances. Fluoropolymers and specifically PVDF are a distinct category of PFAS. In future development, attention should be paid to the choice of those fluoropolymers to ensure they are produced in a sustainable way; preferably without fluorosurfactant; and comply with any new regulation.

## Acknowledgments

Dr. Nicolas Dupré is warmly thanked for helping in the NMR experiments and ARMOR BATTERY FILMS for providing the carbon-coated current collectors.

## References

(1) Armand, M.; Axmann, P.; Bresser, D.; Copley, M.; Edström, K.; Ekberg, C.; Guyomard, D.; Lestriez, B.; Novák, P.; Petranikova, M.; Porcher, W.; Trabesinger, S.; Wohlfahrt-Mehrens, M.; Zhang, H. Lithium-Ion Batteries – Current State of the Art and Anticipated Developments. *Journal of Power Sources* **2020**, *479*, 228708. https://doi.org/10.1016/j.jpowsour.2020.228708.

(2) Dai, Q.; Spangenberger, J.; Ahmed, S.; Gaines, L.; Kelly, J. C.; Wang, M. *EverBatt: A Closed-Loop Battery Recycling Cost and Environmental Impacts Model*; ANL-19/16, 1530874; 2019; p ANL-19/16, 1530874. https://doi.org/10.2172/1530874.

(3) Wood, D. L.; Li, J.; Daniel, C. Prospects for Reducing the Processing Cost of Lithium Ion Batteries. *Journal of Power Sources* **2015**, *275*, 234–242. https://doi.org/10.1016/j.jpowsour.2014.11.019.

(4) Ludwig, B.; Zheng, Z.; Shou, W.; Wang, Y.; Pan, H. Solvent-Free Manufacturing of Electrodes for Lithium-Ion Batteries. *Sci Rep* **2016**, *6* (1), 23150. https://doi.org/10.1038/srep23150.

(5) Liu, Y.; Zhang, R.; Wang, J.; Wang, Y. Current and Future Lithium-Ion Battery Manufacturing. *iScience* **2021**, *24* (4), 102332. https://doi.org/10.1016/j.isci.2021.102332.

(6) El Khakani, S.; Verdier, N.; Lepage, D.; Prébé, A.; Aymé-Perrot, D.; Rochefort, D.; Dollé, M. Melt-Processed Electrode for Lithium Ion Battery. *Journal of Power Sources* **2020**, *454*, 227884. https://doi.org/10.1016/j.jpowsour.2020.227884.

(7) Park, D.-W.; Cañas, N. A.; Wagner, N.; Friedrich, K. A. Novel Solvent-Free Direct Coating Process for Battery Electrodes and Their Electrochemical Performance. *Journal of Power Sources* **2016**, *306*, 758–763. https://doi.org/10.1016/j.jpowsour.2015.12.066.

(8) Verdier, N.; Foran, G.; Lepage, D.; Prébé, A.; Aymé-Perrot, D.; Dollé, M. Challenges in Solvent-Free Methods for Manufacturing Electrodes and Electrolytes for Lithium-Based Batteries. *Polymers* **2021**, *13* (3), 323. https://doi.org/10.3390/polym13030323.

(9) Wang, Z.; Dai, C.; Chen, K.; Wang, Y.; Liu, Q.; Liu, Y.; Ma, B.; Mi, L.; Mao, W. Perspectives on Strategies and Techniques for Building Robust Thick Electrodes for Lithium-Ion Batteries. *Journal of Power Sources* **2022**, *551*, 232176. https://doi.org/10.1016/j.jpowsour.2022.232176.

(10) Li, Y.; Wu, Y.; Wang, Z.; Xu, J.; Ma, T.; Chen, L.; Li, H.; Wu, F. Progress in Solvent-Free Dry-Film Technology for Batteries and Supercapacitors. *Materials Today* **2022**, *55*, 92–109. https://doi.org/10.1016/j.mattod.2022.04.008.

(11) Mitchell, P.; Diego, S.; Zhong, L.; Diego, S.; Xi, X. (54) RECYCLABLE DRY PARTICLE BASED ADHESIVE ELECTRODE AND METHODS OF MAKING SAME.

(12) Xi, X. (75) Inventors: Bin Zou, Chandler, AZ (US); Linda Zhong, San Diego, CA (US); Porter Mitchell, San Diego, CA (US);

(13) Lu, Y.; Zhao, C.-Z.; Yuan, H.; Hu, J.-K.; Huang, J.-Q.; Zhang, Q. Dry Electrode Technology, the Rising Star in Solid-State Battery Industrialization. *Matter* **2022**, *5* (3), 876–898. https://doi.org/10.1016/j.matt.2022.01.011.

(14) Zhang, Y.; Huld, F.; Lu, S.; Jektvik, C.; Lou, F.; Yu, Z. Revisiting Polytetrafluorethylene Binder for Solvent-Free Lithium-Ion Battery Anode Fabrication. *Batteries* **2022**, *8* (6), 57. https://doi.org/10.3390/batteries8060057.

(15) Hippauf, F.; Schumm, B.; Doerfler, S.; Althues, H.; Fujiki, S.; Shiratsuchi, T.; Tsujimura, T.; Aihara, Y.; Kaskel, S. Overcoming Binder Limitations of Sheet-Type Solid-State Cathodes Using a Solvent-Free Dry-Film Approach. *Energy Storage Materials* **2019**, *21*, 390–398. https://doi.org/10.1016/j.ensm.2019.05.033.

(16) Lee, T.; An, J.; Chung, W. J.; Kim, H.; Cho, Y.; Song, H.; Lee, H.; Kang, J. H.; Choi, J. W. Non-Electroconductive Polymer Coating on Graphite Mitigating Electrochemical Degradation of PTFE for a Dry-Processed Lithium-Ion Battery Anode. *ACS Appl. Mater. Interfaces* **2024**, *16* (7), 8930–8938. https://doi.org/10.1021/acsami.3c18862.

(17) Zhang, Y.; Lu, S.; Lou, F.; Yu, Z. Leveraging Synergies by Combining Polytetrafluorethylene with Polyvinylidene Fluoride for Solvent-Free Graphite Anode Fabrication. *Energy Tech* **2022**, *10* (11), 2200732. https://doi.org/10.1002/ente.202200732.

(18) Majeau-Bettez, G.; Hawkins, T. R.; Strømman, A. H. Life Cycle Environmental Assessment of Lithium-Ion and Nickel Metal Hydride Batteries for Plug-In Hybrid and Battery Electric Vehicles. *Environ. Sci. Technol.* **2011**, *45* (10), 4548–4554. https://doi.org/10.1021/es103607c.

(19) Zhen, E.; Jiang, J.; Lv, C.; Huang, X.; Xu, H.; Dou, H.; Zhang, X. Effects of Binder Content on Low-Cost Solvent-Free Electrodes Made by Dry-Spraying Manufacturing for Lithium-Ion Batteries. *Journal of Power Sources* **2021**, *515*, 230644. https://doi.org/10.1016/j.jpowsour.2021.230644.

(20) Wang, M.; Uzun, K.; Frieberg, B. R.; Hu, J.; Li, A.; Huang, X.; Cheng, Y.-T. Influence of Mixing Process on the Performance of Electrodes Made by a Dry Coating Method. *J. Electrochem. Soc.* **2023**, *170* (1), 010541. https://doi.org/10.1149/1945-7111/acb389.

(21) Lv, C.; He, W.; Jiang, J.; Zhen, E.; Dou, H.; Zhang, X. Structure Optimization of Solvent-Free Li4Ti5O12 Electrodes by Electrostatic Spraying for Lithium-Ion Capacitors. *Journal of Power Sources* **2023**, *556*, 232487. https://doi.org/10.1016/j.jpowsour.2022.232487.

(22) Schälicke, G.; Landwehr, I.; Dinter, A.; Pettinger, K.-H.; Haselrieder, W.; Kwade, A. Solvent-Free Manufacturing of Electrodes for Lithium-Ion Batteries via Electrostatic Coating. *Energy Tech* **2020**, *8* (2), 1900309. https://doi.org/10.1002/ente.201900309.

(23) Ludwig, B.; Liu, J.; Chen, I.; Liu, Y.; Shou, W.; Wang, Y.; Pan, H. Understanding Interfacial-Energy-Driven Dry Powder Mixing for Solvent-Free Additive Manufacturing of Li-Ion Battery Electrodes. *Adv Materials Inter* **2017**, *4* (21), 1700570. https://doi.org/10.1002/admi.201700570.

(24) Mohanty, D.; Hockaday, E.; Li, J.; Hensley, D. K.; Daniel, C.; Wood, D. L. Effect of Electrode Manufacturing Defects on Electrochemical Performance of Lithium-Ion Batteries: Cognizance of the Battery Failure Sources. *Journal of Power Sources* **2016**, *312*, 70–79. https://doi.org/10.1016/j.jpowsour.2016.02.007.

(25) Kraytsberg, A.; Ein-Eli, Y. Conveying Advanced Li-Ion Battery Materials into Practice The Impact of Electrode Slurry Preparation Skills. *Adv. Energy Mater.* **2016**, *6* (21), 1600655. https://doi.org/10.1002/aenm.201600655.

(26) Hawley, W. B.; Li, J. Electrode Manufacturing for Lithium-Ion Batteries—Analysis of Current and next Generation Processing. *Journal of Energy Storage* **2019**, *25*, 100862. https://doi.org/10.1016/j.est.2019.100862.

(27) Lenze, G.; Bockholt, H.; Schilcher, C.; Froböse, L.; Jansen, D.; Krewer, U.; Kwade, A. Impacts of Variations in Manufacturing Parameters on Performance of Lithium-Ion-Batteries. *J. Electrochem. Soc.* **2018**, *165* (2), A314–A322. https://doi.org/10.1149/2.1081802jes.

(28) Yonaga, A.; Kawauchi, S.; Mori, Y.; Xuanchen, L.; Ishikawa, S.; Nunoshita, K.; Inoue, G.; Matsunaga, T. Effects of Dry Powder Mixing on Electrochemical Performance of Lithium-Ion Battery Electrode Using Solvent-Free Dry Forming Process. *Journal of Power Sources* **2023**, *581*, 233466. https://doi.org/10.1016/j.jpowsour.2023.233466.

(29) Baranau, V.; Tallarek, U. Random-Close Packing Limits for Monodisperse and Polydisperse Hard Spheres. *Soft Matter* **2014**, *10* (21), 3826. https://doi.org/10.1039/c3sm52959b.

(30) Guy, D.; Lestriez, B.; Bouchet, R.; Guyomard, D. Critical Role of Polymeric Binders on the Electronic Transport Properties of Composites Electrode. *J. Electrochem. Soc.* **2006**, *153* (4), A679. https://doi.org/10.1149/1.2168049.

(31) Seid, K. A.; Badot, J. C.; Dubrunfaut, O.; Levasseur, S.; Guyomard, D.; Lestriez, B. Influence of the Carboxymethyl Cellulose Binder on the Multiscale Electronic Transport in Carbon–LiFePO4 Nanocomposites. *J. Mater. Chem.* **2012**, *22* (45), 24057–24066. https://doi.org/10.1039/C2JM34964G.

(32) Malifarge, S.; Delobel, B.; Delacourt, C. Experimental and Modeling Analysis of Graphite Electrodes with Various Thicknesses and Porosities for High-Energy-Density Li-Ion Batteries. *J. Electrochem. Soc.* **2018**, *165* (7), A1275–A1287. https://doi.org/10.1149/2.0301807jes.

(33) Ni, J.; Yan, Z.; Liu, Y.; Wang, J. Electrical Resistivity Measurements of Surface-Coated Copper Foils. *Materials* **2024**, *17* (12), 2951. https://doi.org/10.3390/ma17122951.

(34) Wang, C.-W.; Sastry, A. M.; Striebel, K. A.; Zaghib, K. Extraction of Layerwise Conductivities in Carbon-Enhanced, Multilayered LiFePO4 Cathodes. *Journal of The Electrochemical Society* **2005**, *152* (5), A1001. https://doi.org/10.1149/1.1890766.

(35) MatWeb Database. Overview of Materials for Polyvinylidinefluoride (PVDF), Molded/Extruded. www.matweb.com/search/datasheet_print.aspx?matguid=a011f8ccf4b448a19246773a32085094 (accessed 2023-11-23).

(36) Oku, T.; Kurumada, A.; Imamura, Y.; Ishihara, M. Effects of Ion Irradiation on the Hardness Properties of Graphites and C/C Composites by Indentation Tests. *Journal of Nuclear Materials* **2008**, *381* (1–2), 92–97. https://doi.org/10.1016/j.jnucmat.2008.07.026.

(37) Park, Y.-S.; Oh, E.-S.; Lee, S.-M. Effect of Polymeric Binder Type on the Thermal Stability and Tolerance to Roll-Pressing of Spherical Natural Graphite Anodes for Li-Ion Batteries. *Journal of Power Sources* **2014**, *248*, 1191–1196. https://doi.org/10.1016/j.jpowsour.2013.10.076.

(38) Diener, A.; Ivanov, S.; Haselrieder, W.; Kwade, A. Evaluation of Deformation Behavior and Fast Elastic Recovery of Lithium-Ion Battery Cathodes via Direct Roll-Gap Detection During Calendering. *Energy Technology* **2022**, *10* (4), 2101033. https://doi.org/10.1002/ente.202101033.

(39) De Freitas, S. T.; Sinke, J. Test Method to Assess Interface Adhesion in Composite Bonding. *Appl Adhes Sci* **2015**, *3* (1), 9. https://doi.org/10.1186/s40563-015-0033-5.

(40) Gaikwad, A. M.; Arias, A. C. Understanding the Effects of Electrode Formulation on the Mechanical Strength of Composite Electrodes for Flexible Batteries. *ACS Appl. Mater. Interfaces* **2017**, *9* (7), 6390–6400. https://doi.org/10.1021/acsami.6b14719.

(41) *Adhesive Joints: Formation, Characteristics and Testing, Volume 2: Proceedings of the Second International Symposium on Adhesive Joints: Formation, Characteristics and Testing Held under*

*the Aegis of MST Conferences in Newark, New Jersey, May 22 - 24, 2000*; Mittal, K. L., Ed.; VSP: Utrecht, 2002.

(42) Creton, C.; Kramer, E. J.; Brown, H. R.; Hui, C.-Y. Adhesion and Fracture of Interfaces Between Immiscible Polymers: From the Molecular to the Continuum Scale.

(43) Landesfeind, J.; Hattendorff, J.; Ehrl, A.; Wall, W. A.; Gasteiger, H. A. Tortuosity Determination of Battery Electrodes and Separators by Impedance Spectroscopy. *J. Electrochem. Soc.* **2016**, *163* (7), A1373–A1387. https://doi.org/10.1149/2.1141607jes.

(44) Landesfeind, J.; Eldiven, A.; Gasteiger, H. A. Influence of the Binder on Lithium Ion Battery Electrode Tortuosity and Performance. *J. Electrochem. Soc.* **2018**, *165* (5), A1122–A1128. https://doi.org/10.1149/2.0971805jes.

(45) Zacharias, N. A.; Nevers, D. R.; Skelton, C.; Knackstedt, K.; Stephenson, D. E.; Wheeler, D. R. Direct Measurements of Effective Ionic Transport in Porous Li-Ion Electrodes. *Journal of The Electrochemical Society* **2012**, *160* (2), A306. https://doi.org/10.1149/2.062302jes.

(46) Tambio, S. J.; Cadiou, F.; Maire, E.; Besnard, N.; Deschamps, M.; Lestriez, B. The Concept of Effective Porosity in the Discharge Rate Performance of High-Density Positive Electrodes for Automotive Application. *J. Electrochem. Soc.* **2020**, *167* (16), 160509. https://doi.org/10.1149/1945-7111/abcb42.

(47) Park, J.; Suh, S.; Tamulevičius, S.; Kim, D.; Choi, D.; Jeong, S.; Kim, H.-J. Practical Approaches to Apply Ultra-Thick Graphite Anode to High-Energy Lithium-Ion Battery: Carbonization and 3-Dimensionalization. *Nanomaterials* **2022**, *12* (15), 2625. https://doi.org/10.3390/nano12152625.

(48) Buqa, H.; Holzapfel, M.; Krumeich, F.; Veit, C.; Novák, P. Study of Styrene Butadiene Rubber and Sodium Methyl Cellulose as Binder for Negative Electrodes in Lithium-Ion Batteries. *Journal of Power Sources* **2006**, *161* (1), 617–622. https://doi.org/10.1016/j.jpowsour.2006.03.073.

(49) Buqa, H.; Goers, D.; Holzapfel, M.; Spahr, M. E.; Novák, P. High Rate Capability of Graphite Negative Electrodes for Lithium-Ion Batteries. *J. Electrochem. Soc.* **2005**, *152* (2), A474. https://doi.org/10.1149/1.1851055.

(50) Chen, K.-H.; Namkoong, M. J.; Goel, V.; Yang, C.; Kazemiabnavi, S.; Mortuza, S. M.; Kazyak, E.; Mazumder, J.; Thornton, K.; Sakamoto, J.; Dasgupta, N. P. Efficient Fast-Charging of Lithium-Ion Batteries Enabled by Laser-Patterned Three-Dimensional Graphite Anode Architectures. *Journal of Power Sources* **2020**, *471*, 228475. https://doi.org/10.1016/j.jpowsour.2020.228475.

(51) Parmananda, M.; Norris, C.; Roberts, S. A.; Mukherjee, P. P. Probing the Role of Multi-Scale Heterogeneity in Graphite Electrodes for Extreme Fast Charging.

(52) Hu, J.; Zhong, S.; Yan, T. Using Carbon Black to Facilitate Fast Charging in Lithium-Ion Batteries. *Journal of Power Sources* **2021**, *508*, 230342. https://doi.org/10.1016/j.jpowsour.2021.230342.

(53) Besnard, N.; Etiemble, A.; Douillard, T.; Dubrunfaut, O.; Tran-Van, P.; Gautier, L.; Franger, S.; Badot, J.; Maire, E.; Lestriez, B. Multiscale Morphological and Electrical Characterization of Charge Transport Limitations to the Power Performance of Positive Electrode Blends for Lithium-Ion Batteries. *Advanced Energy Materials* **2017**, *7* (8), 1602239. https://doi.org/10.1002/aenm.201602239.

(54) Usseglio-Viretta, F. L. E.; Colclasure, A.; Mistry, A. N.; Claver, K. P. Y.; Pouraghajan, F.; Finegan, D. P.; Heenan, T. M. M.; Abraham, D.; Mukherjee, P. P.; Wheeler, D.; Shearing, P.; Cooper, S. J.; Smith, K. Resolving the Discrepancy in Tortuosity Factor Estimation for Li-Ion

Battery Electrodes through Micro-Macro Modeling and Experiment. *J. Electrochem. Soc.* **2018**, *165* (14), A3403–A3426. https://doi.org/10.1149/2.0731814jes.

(55) Landesfeind, J.; Ebner, M.; Eldiven, A.; Wood, V.; Gasteiger, H. A. Tortuosity of Battery Electrodes: Validation of Impedance-Derived Values and Critical Comparison with 3D Tomography. *J. Electrochem. Soc.* **2018**, *165* (3), A469–A476. https://doi.org/10.1149/2.0231803jes.

(56) Wu, J.; Ju, Z.; Zhang, X.; Xu, X.; Takeuchi, K. J.; Marschilok, A. C.; Takeuchi, E. S.; Yu, G. Low-Tortuosity Thick Electrodes with Active Materials Gradient Design for Enhanced Energy Storage. *ACS Nano* **2022**, *16* (3), 4805–4812. https://doi.org/10.1021/acsnano.2c00129.

(57) Grillet, A. M.; Humplik, T.; Stirrup, E. K.; Roberts, S. A.; Barringer, D. A.; Snyder, C. M.; Janvrin, M. R.; Apblett, C. A. Conductivity Degradation of Polyvinylidene Fluoride Composite Binder during Cycling: Measurements and Simulations for Lithium-Ion Batteries. *J. Electrochem. Soc.* **2016**, *163* (9), A1859–A1871. https://doi.org/10.1149/2.0341609jes.

(58) Pouraghajan, F.; Thompson, A. I.; Hunter, E. E.; Mazzeo, B.; Christensen, J.; Subbaraman, R.; Wray, M.; Wheeler, D. The Effects of Cycling on Ionic and Electronic Conductivities of Li –Ion Battery Electrodes. *Journal of Power Sources* **2021**, *492*, 229636. https://doi.org/10.1016/j.jpowsour.2021.229636.

(59) Winter, M.; Besenhard, J. O.; Spahr, M. E.; Novák, P. Insertion Electrode Materials for Rechargeable Lithium Batteries. *Adv. Mater.* **1998**, *10* (10), 725–763. https://doi.org/10.1002/(SICI)1521-4095(199807)10:10<725::AID-ADMA725>3.0.CO;2-Z.

(60) Huff, L. A.; Tavassol, H.; Esbenshade, J. L.; Xing, W.; Chiang, Y.-M.; Gewirth, A. A. Identification of Li-Ion Battery SEI Compounds through $^{7}$Li and $^{13}$C Solid-State MAS NMR Spectroscopy and MALDI-TOF Mass Spectrometry. *ACS Appl. Mater. Interfaces* **2016**, *8* (1), 371–380. https://doi.org/10.1021/acsami.5b08902.

(61) Michael, H.; Iacoviello, F.; Heenan, T. M. M.; Llewellyn, A.; Weaving, J. S.; Jervis, R.; Brett, D. J. L.; Shearing, P. R. A Dilatometric Study of Graphite Electrodes during Cycling with X-Ray Computed Tomography. *J. Electrochem. Soc.* **2021**, *168* (1), 010507. https://doi.org/10.1149/1945-7111/abd648.

(62) Chang, C. C, Chen, T. K, Chen, L. C, Her, L. J.; Hong, J. L. The Influence of Different Electrode Fabrication Methods and Poly(Vinylidene Fluoride) Binders on the Anode Electrode Dimension Stability and Cyclability in Lithium-Ion Batteries, 2008, *11*.

(63) Yoo, M.; Frank, C. W.; Mori, S.; Yamaguchi, S. Effect of Poly(Vinylidene Fluoride) Binder Crystallinity and Graphite Structure on the Mechanical Strength of the Composite Anode in a Lithium Ion Battery. *Polymer* **2003**, *44* (15), 4197–4204. https://doi.org/10.1016/S0032-3861(03)00364-1.

(64) Wendt, C.; Niehoff, P.; Winter, M.; Schappacher, F. M. Determination of the Mechanical Integrity of Polyvinylidene Difluoride in LiNi1/3Co1/3Mn1/3O2 Electrodes for Lithium Ion Batteries by Use of the Micro-Indentation Technique. *Journal of Power Sources* **2018**, *391*, 80–85. https://doi.org/10.1016/j.jpowsour.2018.03.064.

## Tables

**Table I.** PVdF distribution as agglomerates or as primary particles at the surface of graphite based on mixing time.

| Mixture | $\chi_{Gr,PVdF}$ Fraction of graphite surface covered by PVdF | $D_{agglo}$ Mean PVdF agglomerate diameter (μm) | $\chi_{PVdF,Gr}$ Fraction of PVdF present in graphite's surface | $\chi_{PVdF,agglo}$ Fraction of PVdF forming agglomerates | $N_{PVdF\ per\ agglo}$ Mean number of PVdF particles consitituting one agglomerate | $N_{agglo}$ Number of PVdF agglomerates per g of electrode powder mixture |
|---|---|---|---|---|---|---|
| 1-SM | 0.23 ± 0.03 | 4.84 ± 1.49 | 0.42 ± 0.06 | 0.58 ± 0.06 | 3696 ± 1221 | $2.6 \times 10^8 \pm 1.1 \times 10^8$ |
| 3-MM | 0.34 ± 0.06 | 3.42 ± 0.86 | 0.63 ± 0.12 | 0.37 ± 0.12 | 1310 ± 323 | $4.8 \times 10^8 \pm 1.4 \times 10^8$ |
| 15-LM | 0.45 ± 0.07 | 3.34 ± 0.22 | 0.83 ± 0.13 | 0.17 ± 0.13 | 1226 ± 244 | $2.3 \times 10^8 \pm 0.4 \times 10^8$ |

**Table II.** Electrodes technical information

| Electrode | Mass loading (mg $cm^{-2}$) | Porosity (%) | Thickness (μm) | Density (g $cm^{-3}$) |
|---|---|---|---|---|
| 1-DSE | 12.6 | 26 | 81.2 ± 3.4 | 1.54 |
| 3-DSE | 12.4 | 26 | 80.0 ± 2.6 | 1.55 |
| 15-DSE | 14.9 | 27 | 98.0 ± 1.9 | 1.51 |
| WSE | 12.7 | 25 | 82.4 ± 1.1 | 1.54 |

**Table III.** Indentation measurements for pristine and cycled electrodes: hardness (H), elastic modulus (E), elastic work ($W_{elast}$), plastic work ($W_{plast}$), total work ($W_{total}$), ratio of plastic work to total work ($h_{plast}$). Δ (%) is calculated from the difference between the cycled and pristine value, normalized by pristine value.

| Electrode | H (MPa) | E (MPa) | $W_{elast}$ (nJ) | $W_{plast}$ (nJ) | $W_{total}$ (nJ) | $\eta_{plast}$ (%) |
|---|---|---|---|---|---|---|
| 1-DSE | | | | | | |
| **Pristine** | **13.3 ± 2.8** | **0.65 ± 0.25** | **75 ± 5** | **308 ± 30** | **383 ± 25** | **80.3 ± 2.5** |
| Cycled | 14.3 ± 5.4 | 1.64 ± 0.48 | 27 ± 0 | 355 ± 60 | 381 ± 60 | 92.9 ± 0.6 |
| Δ (%) | +7 | +150 | -65 | +15 | -0.5 | +16 |
| 3-DSE | | | | | | |
| **Pristine** | **5.1 ± 0.5** | **0.34 ± 0.03** | **65 ± 3** | **342 ± 20** | **408 ± 20** | **84.0 ± 0.2** |
| Cycled | 13.0 ± 2.2 | 1.42 ± 0.30 | 35 ± 10 | 391 ± 60 | 426 ± 60 | 91.8 ± 2.0 |
| Δ (%) | +153 | +316 | -47 | +14 | +4 | +9 |
| 15-DSE | | | | | | |
| **Pristine** | **4.7 ± 0.5** | **0.31 ± 0.03** | **76 ± 3** | **386 ± 20** | **462 ± 20** | **83.5 ± 0.5** |
| Cycled | 19.2 ± 13.1 | 1.91 ± 0.65 | 28 ± 10 | 341 ± 90 | 369 ± 10 | 92.1 ± 1.6 |
| Δ(%) | +309 | +517 | -63 | -12 | -20 | +10 |
| WSE | | | | | | |
| **Pristine** | **6.8 ± 0.6** | **0.46 ± 0.04** | **79 ± 5** | **345 ± 20** | **425 ± 25** | **81.4 ± 0.6** |
| Cycled | 12.7 ± 1.5 | 1.39 ± 0.18 | 34 ± 1 | 413 ± 37 | 447 ± 37 | 92.4 ± 0.5 |
| Δ(%) | +87 | +200 | -57 | +20 | +5 | +14 |

**Table IV.** Tortuosity factor determination electrodes technical information

| Electrode | Mean mass loading (mg $cm^{-2}$) | Mean porosity (%) | Tortuosity factor |
|---|---|---|---|
| 1- DSE | 13.1 | 28 | 3.17 |
| 3- DSE | 14.2 | 25 | 3.79 |
| 15- DSE | 13.8 | 27 | 3.16 |
| WSE | 13.0 | 31 | 6.94 |

**Figure Captions**

***Figure 1.*** Schema of the electrode fabrication process: (a) dry-mixing of electrode components, (b) electrostatic dry spray-coating of electrode powder onto a metallic current collector and (c) calendering at high temperature and consolidation of electrode, (d) consolidated electrode with good homogeneity and flexibility is shown.

***Figure 2.*** SEM images of graphite particles covered by PVdF. Next to the SEM images, we observe a schematic representation of the particles in the mixtures, the black spheres represent graphite and the white ones represent PVdF. (a-c) corresponds to 1-SM, (d-f) corresponds to 3-MM and (g-i) corresponds to 15-LM. PVdF agglomerates are slightly highlighted in blue.

***Figure 3.*** (a) Schema of the electrode powder mixture resistivity measurements, (b) a plot of the powder density obtained (in $g \cdot cm^{-3}$) as a function of the pressure (in MPa) applied for the different powder mixtures, (c) a plot of the resistivity as a function of the density ($g \cdot cm^{-3}$), and d) mean resistivity for densities between 1.6 and 1.77 g $cm^{-3}$, as a function of the fraction of graphite surface covered by PVdF particles ($\chi_{Gr,PVdF}$).

***Figure 4.*** Cross-section SEM images and EDS analysis of DSEs with a short 1-DSE (a-c), moderate 3-DSE (d-f) and long 15-DSE (g-i) mixing time. Reference WSE is represented in images j-l. The images a, d, g, and j show the distribution analysis of fluorine (F) or sodium (Na) superimposed to the cross-section image of the correspondant electrode. Images b, e, h, and l, on the other hand, represent solely the EDS mapping of fluorine and sodium. The images c, f, I, and l are zooms on the cross section images.

***Figure 5.*** (a) Four-point probe ohmic resistivity (in $m\Omega \cdot cm$) for 1-DSE, 3-DSE, 15-DSE and WSE. (b) Ohmic resistivity (in $m\Omega \cdot cm$) as a function of the fraction of graphite surface covered by PVdF ($\chi_{Gr,PVdF}$).

***Figure 6.*** (a) H and E values as a function of the fraction of graphite surface covered by PVdF ($\chi_{Gr,PVdF}$), (b) $W_{total}$, $W_{elast}$, $W_{plastic}$ as a function of graphite surface covered by PVdF ($\chi_{Gr,PVdF}$), (c) peel strength obtained for our three DSE and (d) peel strength as a function of the number of PVdF agglomerates per g of electrode powder mixture ($N_{agglo}$).

***Figure 7.*** (a) Rate capability evaluation (capacity at different current intensity rates of charge/delithiation) followed by (b) long-term cycling measurements at a lithiation/delithiation C-rate of 0.2C in half-cell coin cell format. (c) Long-term cycling evaluation of the electrodes in full-cell pouch format over 150 cycles at a 0.2C rate.

***Figure 8.*** dQ/dV peaks position (V) evolution with cycle number for (a) lithiation or discharge and (b) delithiation or charge of graphite.

***Figure 9.*** Four-point probe ohmic resistivity (in mΩ-cm) for the pristine electrodes (solid fill) and the electrodes after cycling (patterned fill).

***Figure 10.*** (a) Mean cell polarization of the cell between the $5^{th}$ and the $80^{th}$ cycle, and delithiation capacity measured at 2C rate vs the fraction of graphite surface covered by PVdF ($\chi_{Gr,PVdF}$). (b) Capacity retention (half-cell coin cell format) after the $100^{th}$ cycle vs peel strength (N/m).

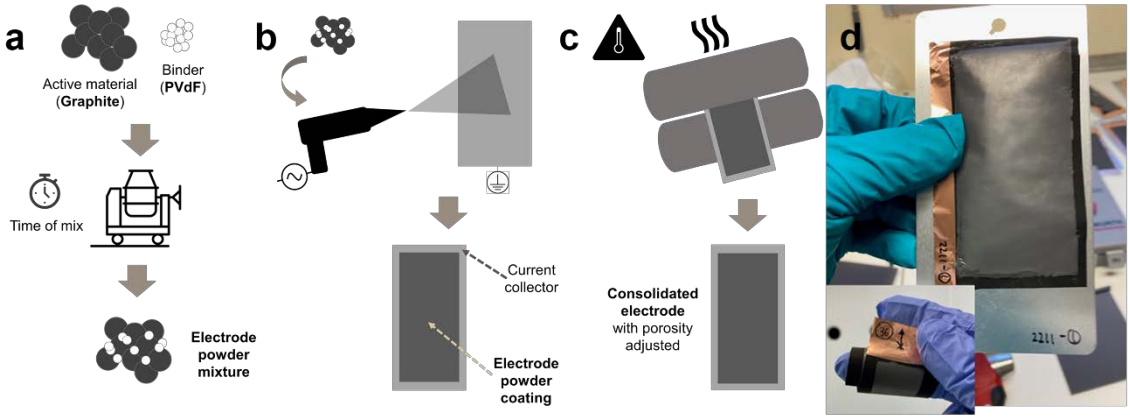


***Figure 1.*** Schema of the electrode fabrication process: (a) dry-mixing of electrode components, (b) electrostatic dry spray-coating of electrode powder onto a metallic current collector and (c) calendering at high temperature and consolidation of electrode, (d) consolidated electrode with good homogeneity and flexibility is shown.

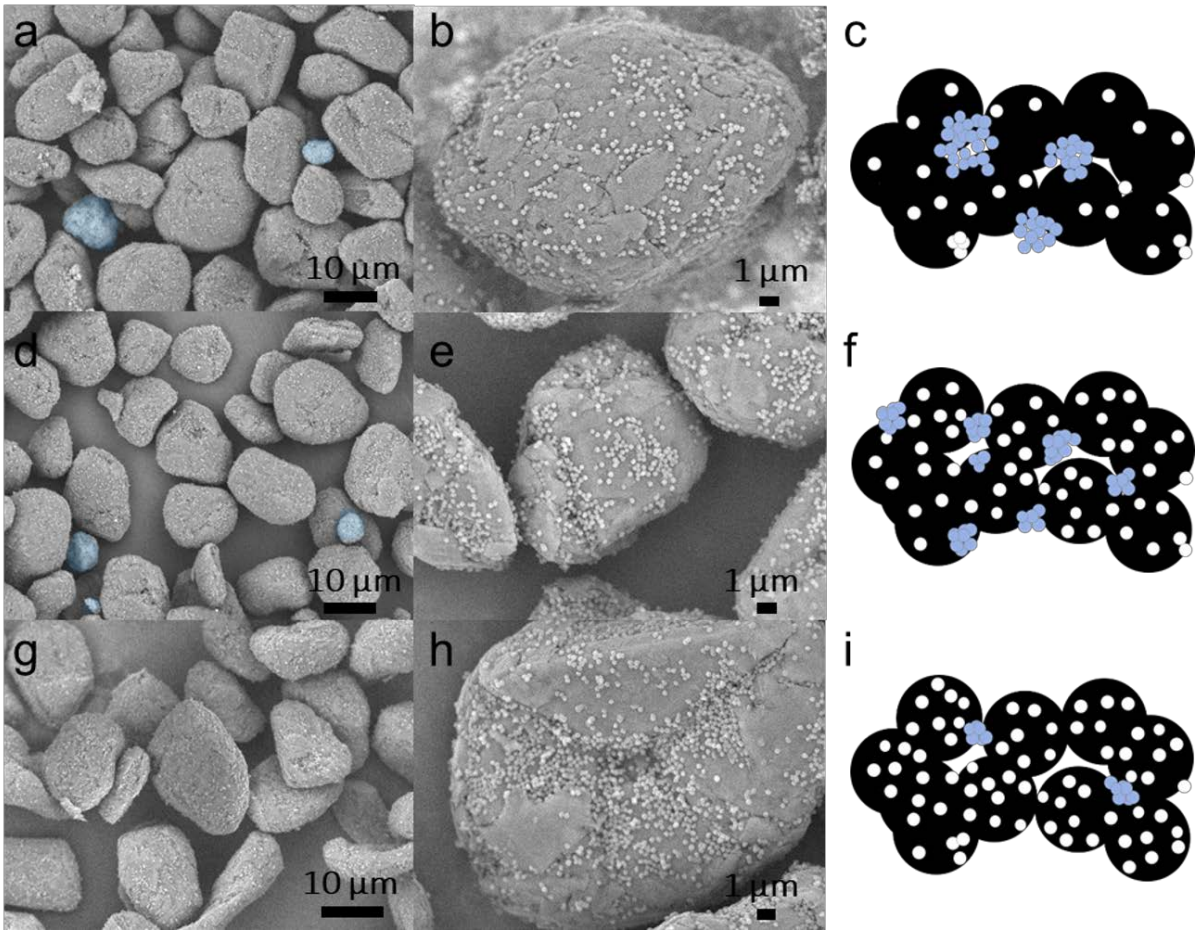


***Figure 2.*** SEM images of graphite particles covered by PVdF. Next to the SEM images, we observe a schematic representation of the particles in the mixtures, the black spheres represent graphite and the white ones represent PVdF. (a-c) corresponds to 1-SM, (d-f) corresponds to 3-MM and (g-i) corresponds to 15-LM. PVdF agglomerates are slightly highlighted in blue.

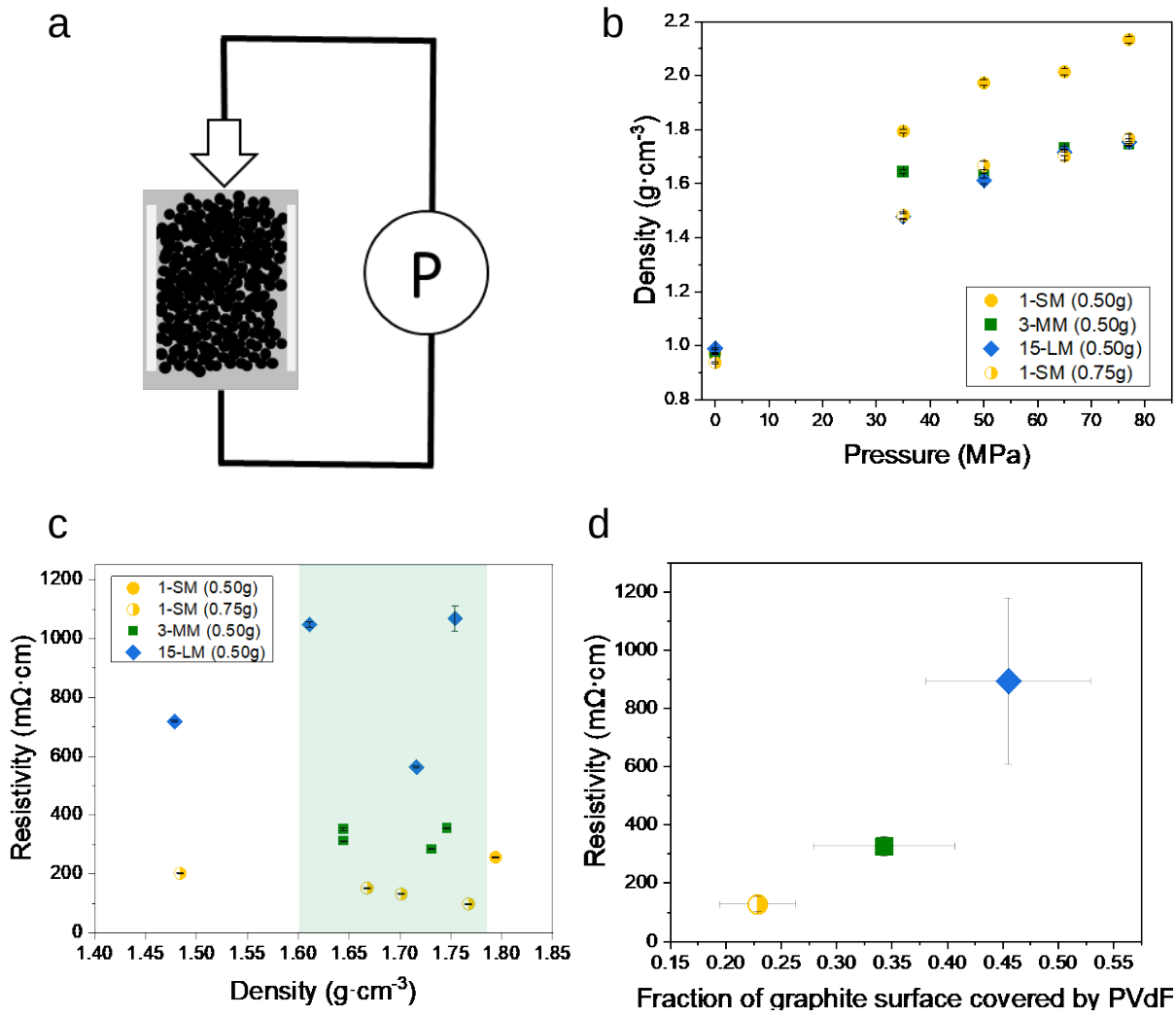


***Figure 3.*** (a) Schema of the electrode powder mixture resistivity measurements, (b) a plot of the powder density obtained (in g·cm$^{-3}$) as a function of the pressure (in MPa) applied for the different powder mixtures, (c) a plot of the resistivity as a function of the density (g·cm$^{-3}$), and d) mean resistivity for densities between 1.6 and 1.77 g cm$^{-3}$, as a function of the fraction of graphite surface covered by PVdF particles ($\chi_{Gr,PVdF}$).

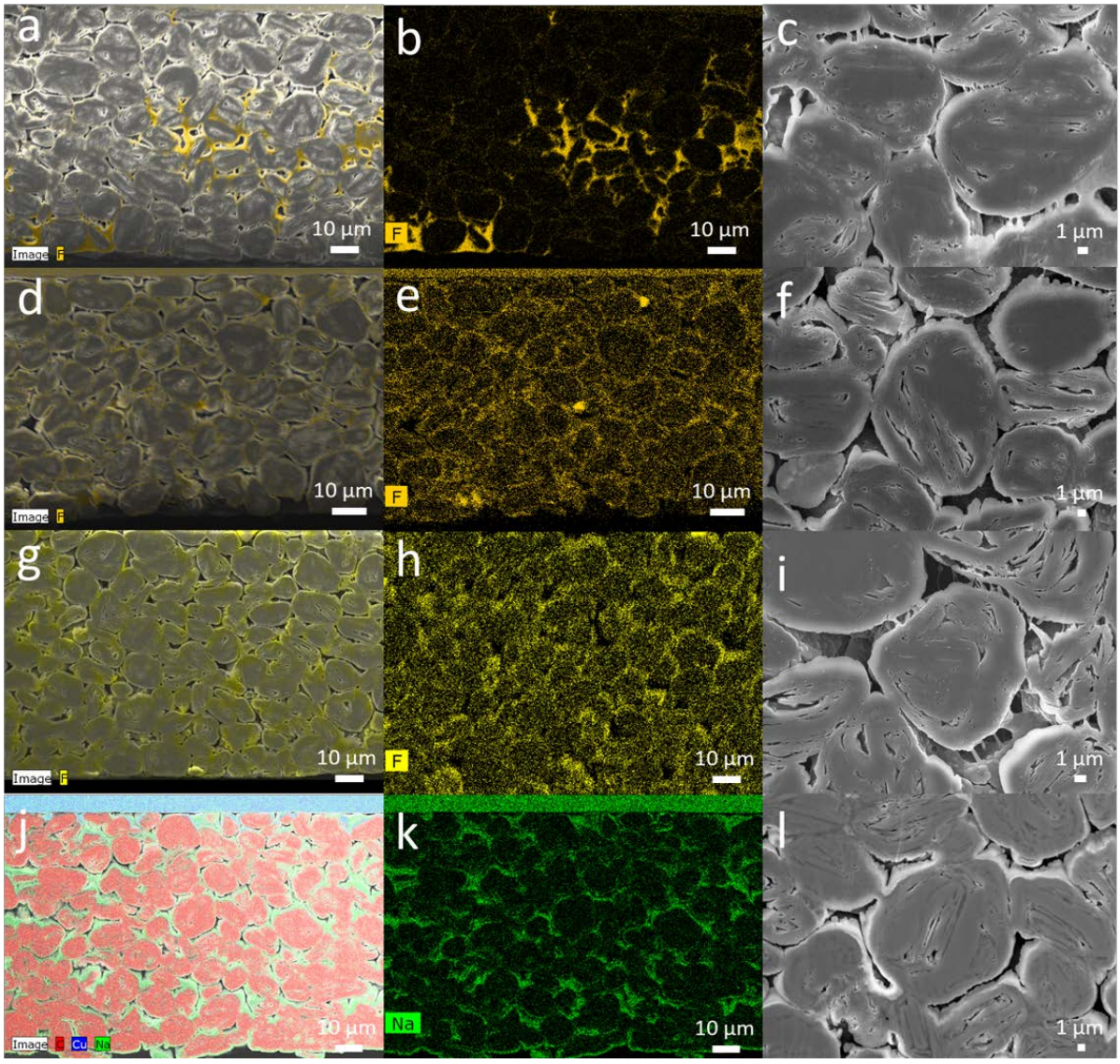


***Figure 4.*** Cross-section SEM images and EDS analysis of DSEs with a short 1-DSE (a-c), moderate 3-DSE (d-f) and long 15-DSE (g-i) mixing time. Reference WSE is represented in images j-l. The images a, d, g, and j show the distribution analysis of fluorine (F) or sodium (Na) superimposed to the cross-section image of the correspondant electrode. Images b, e, h, and l, on the other hand, represent solely the EDS mapping of fluorine and sodium. The images c, f, I, and l are zooms on the cross section images.

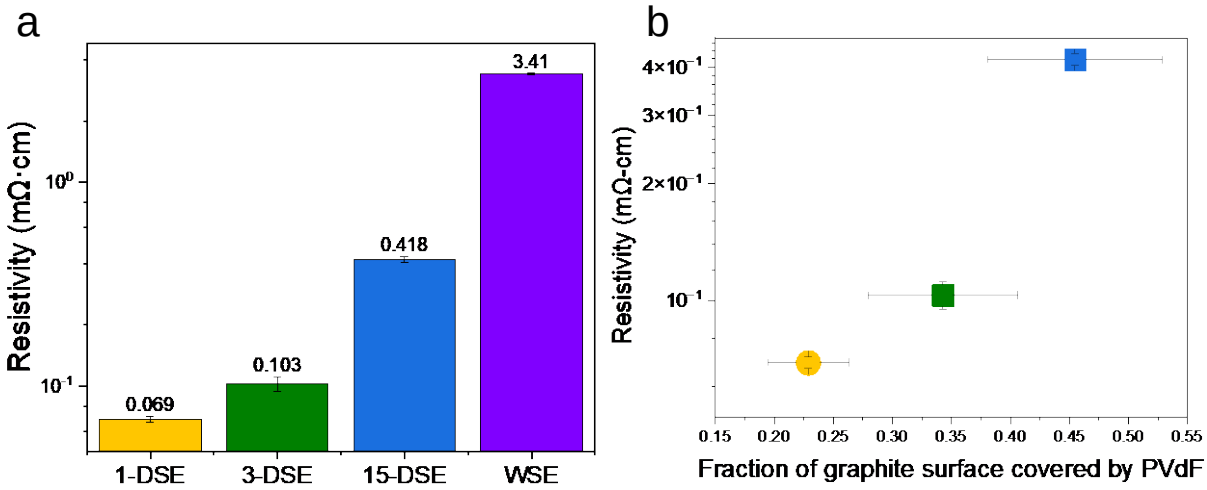


***Figure 5.*** (a) Four-point probe ohmic resistivity (in mΩ·cm) for 1-DSE, 3-DSE, 15-DSE and WSE. (b) Ohmic resistivity (in mΩ·cm) as a function of the fraction of graphite surface covered by PVdF ($\chi_{Gr,PVdF}$).

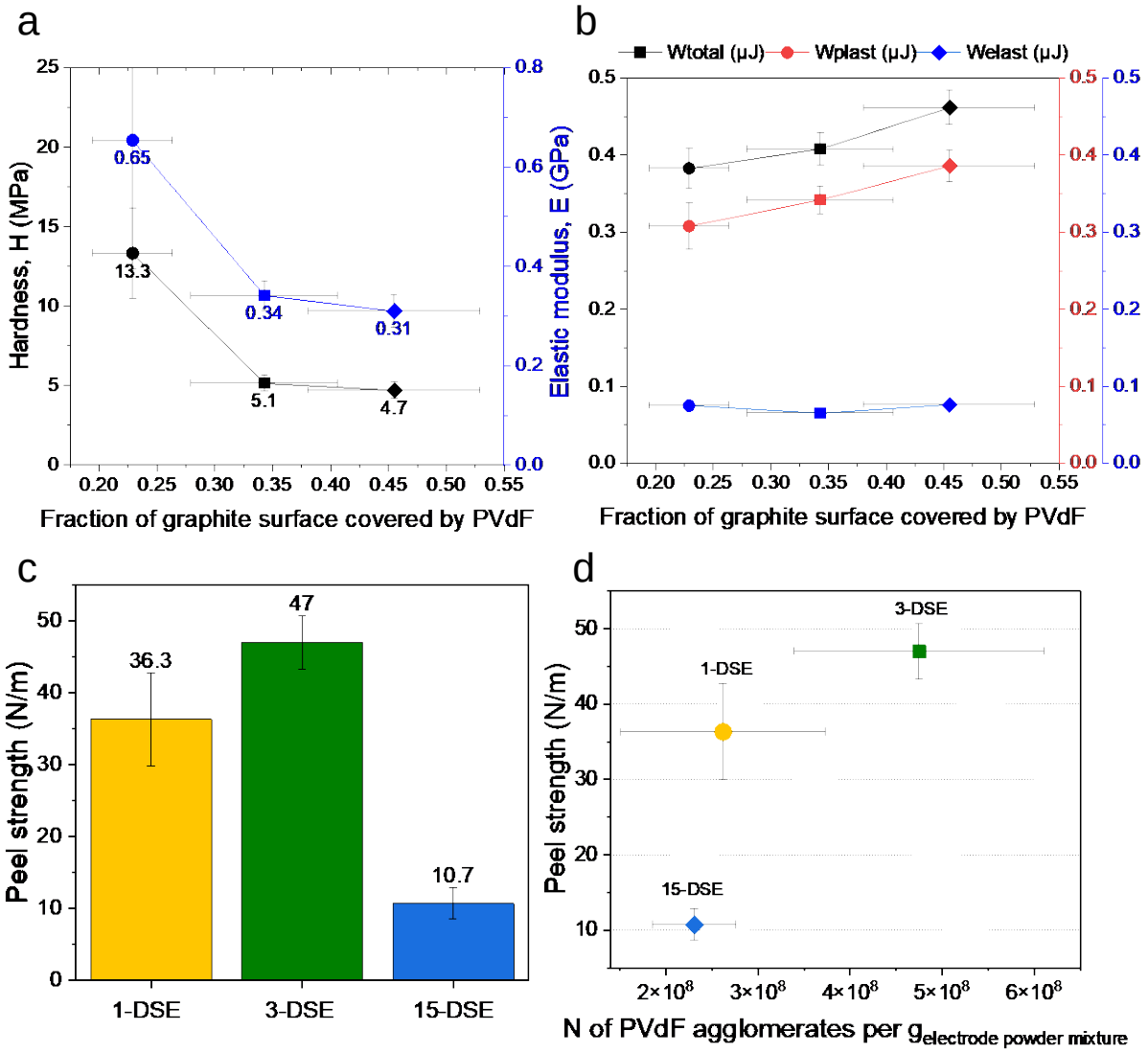


***Figure 6.*** (a) H and E values as a function of the fraction of graphite surface covered by PVdF ($\chi_{Gr,PVdF}$), (b) $W_{total}$, $W_{elast}$, $W_{plastic}$ as a function of graphite surface covered by PVdF ($\chi_{Gr,PVdF}$), (c) peel strength obtained for our three DSE and (d) peel strength as a function of the number of PVdF agglomerates per g of electrode powder mixture ($N_{agglo}$).

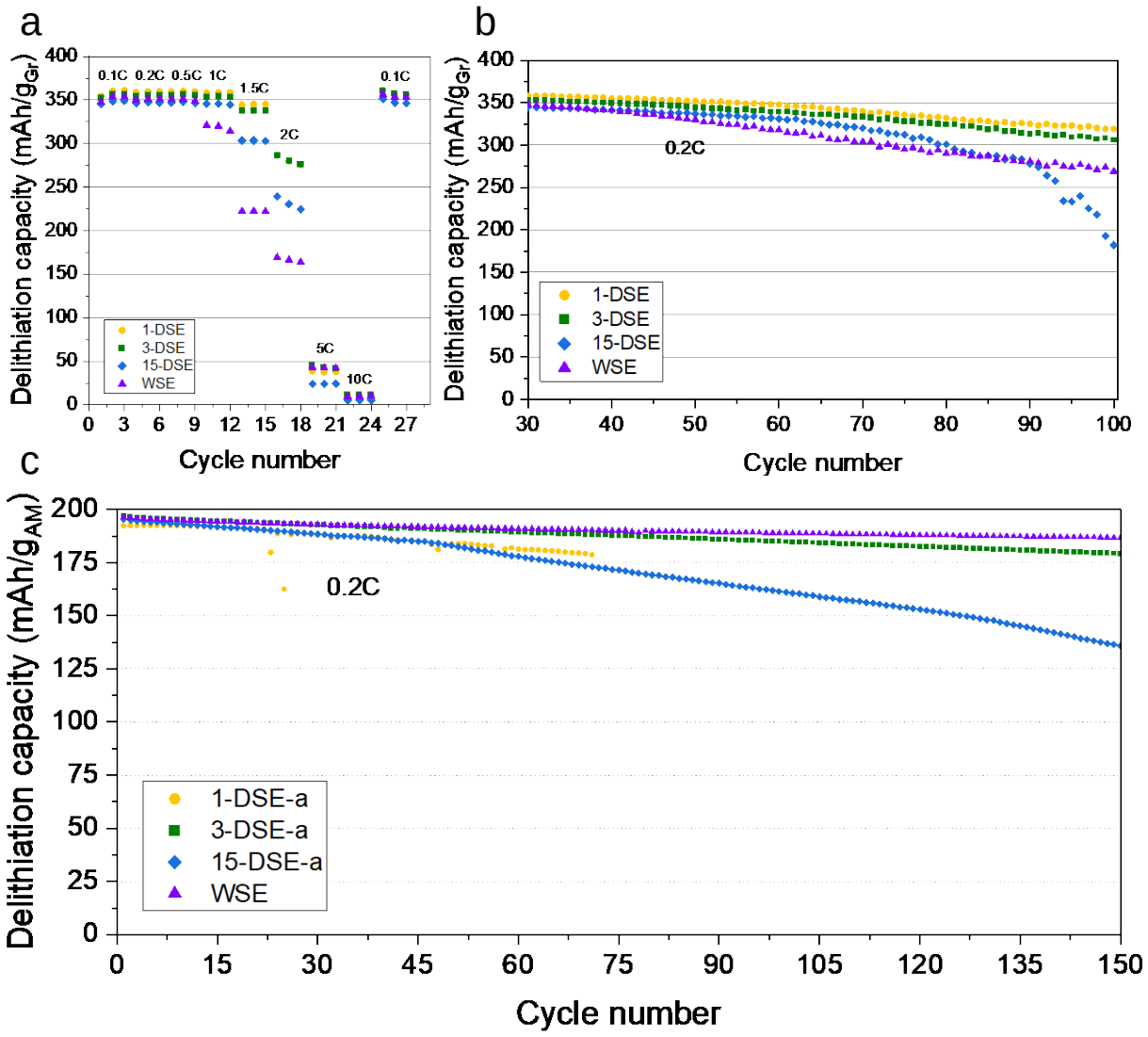


***Figure 7.*** (a) Rate capability evaluation (capacity at different current intensity rates of charge/delithiation) followed by (b) long-term cycling measurements at a lithiation/delithiation C-rate of 0.2C in half-cell coin cell format. (c) Long-term cycling evaluation of the electrodes in full-cell pouch format over 150 cycles at a 0.2C rate.

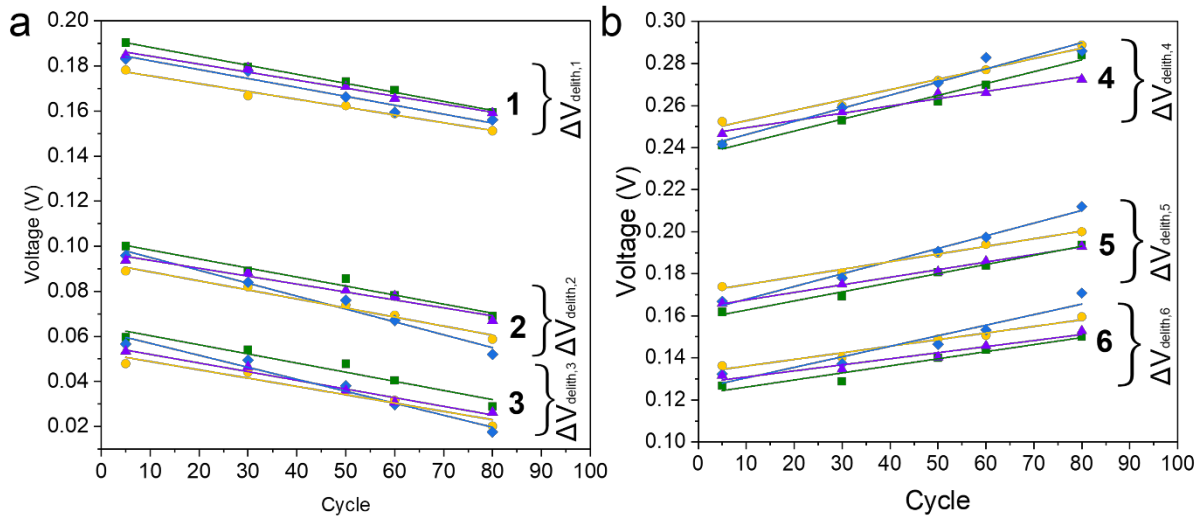


***Figure 8.*** dQ/dV peaks position (V) evolution with cycle number for (a) lithiation or discharge and (b) delithiation or charge of graphite.

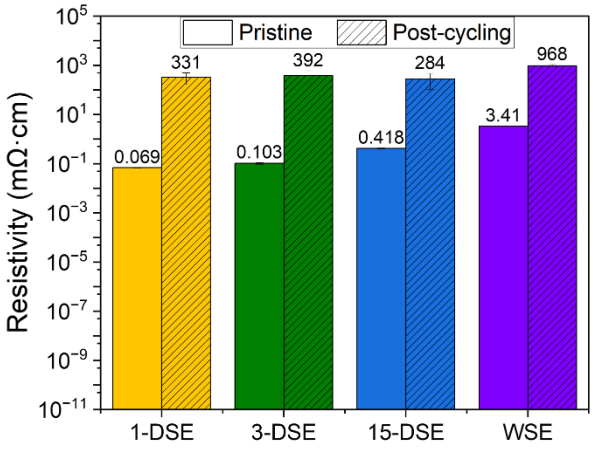


***Figure 9.*** Four-point probe ohmic resistivity (in mΩ-cm) for the pristine electrodes (solid fill) and the electrodes after cycling (patterned fill).

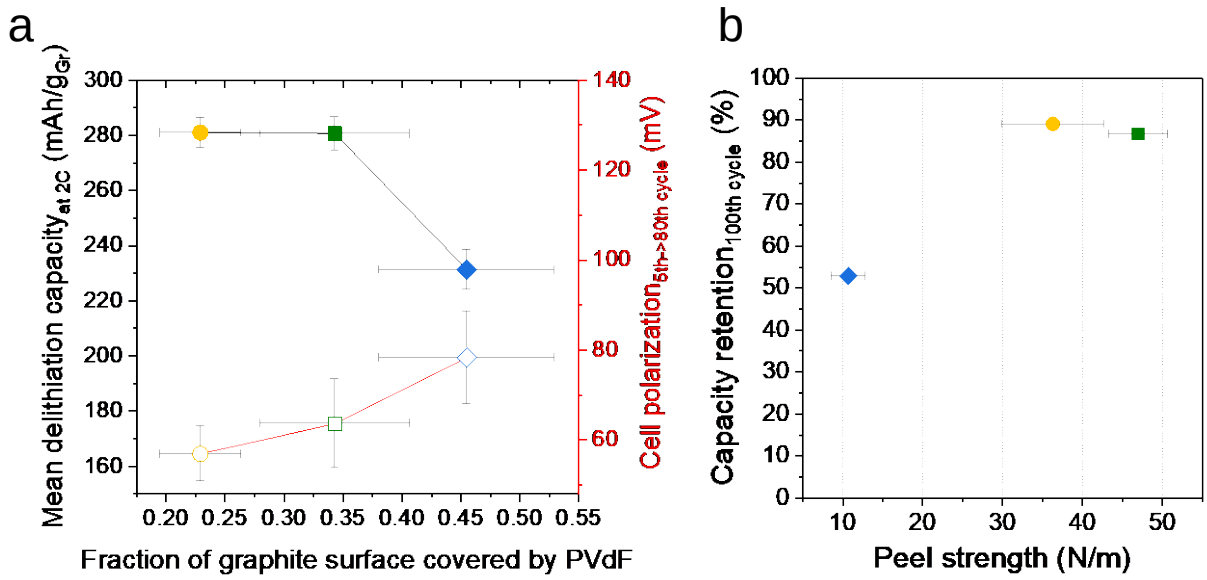


***Figure 10.*** (a) Mean cell polarization of the cell between the 5$^{th}$ and the 80$^{th}$ cycle, and delithiation capacity measured at 2C rate vs the fraction of graphite surface covered by PVdF ($\chi_{Gr,PVdF}$). (b) Capacity retention (half-cell coin cell format) after the 100$^{th}$ cycle vs peel strength (N/m).

**Supplementary information for**

# Effect of PVdF distribution on properties and performance of dry spray-coated graphite electrodes for lithium-ion batteries for electric vehicle applications

**Authors:** Jesus Alberto Barreras-Uruchurtu,[1,2] Nicolas Besnard,[2] Clément Paul,[3] Lauréline Marchal,[3] Samuel Devisme,[3] Bernard Lestriez[1]

[1] Nantes Université, CNRS, Institut des Matériaux de Nantes Jean Rouxel, IMN, Nantes F-44000, France

[2] Ampere (Renault Group), Technocentre, 1 avenue du Golf, 78288 Guyancourt, France

[3] Arkema, Centre de recherche, développement, applications et technique de l'ouest (CERDATO) Serquigny, France

[4] Arkema, Centre de Recherche Rhône-Alpes (CRRA) Lyon, France

## Electrode powder mixtures

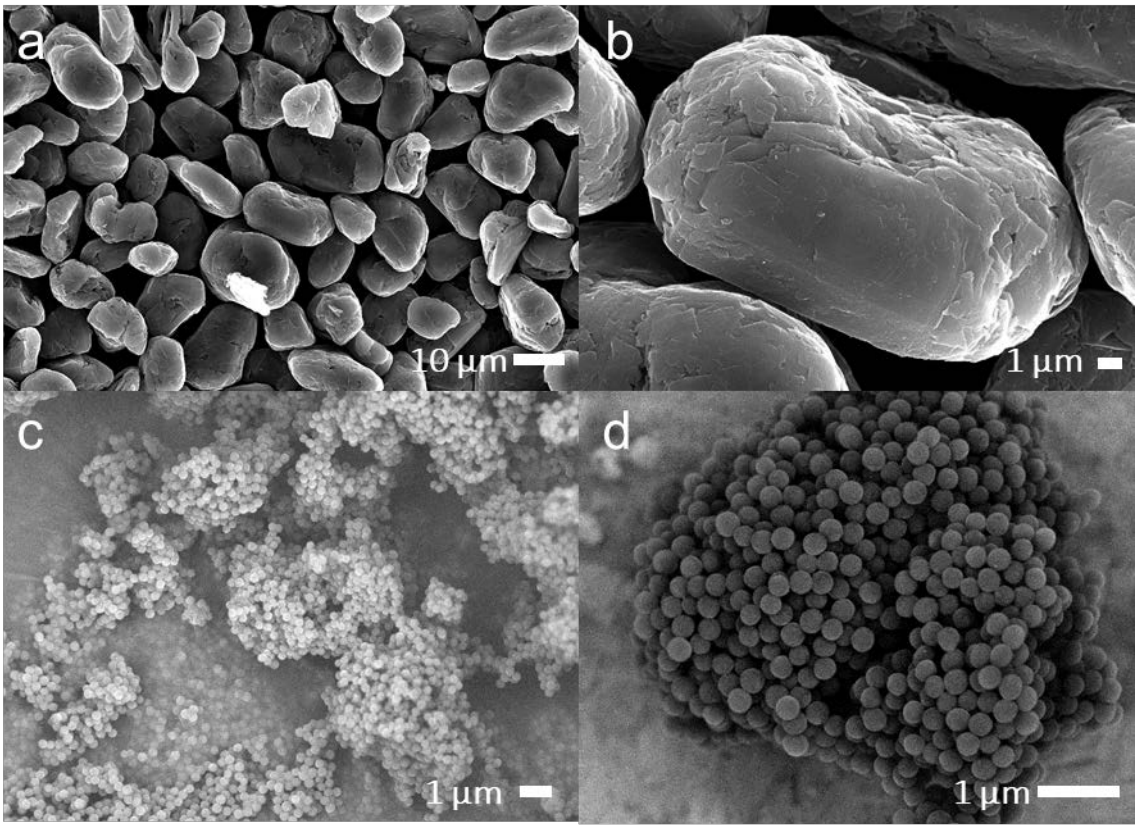


***Figure S1.*** SEM images of (a-b) pristine graphite particles and (c-d) pristine PVdF agglomerates

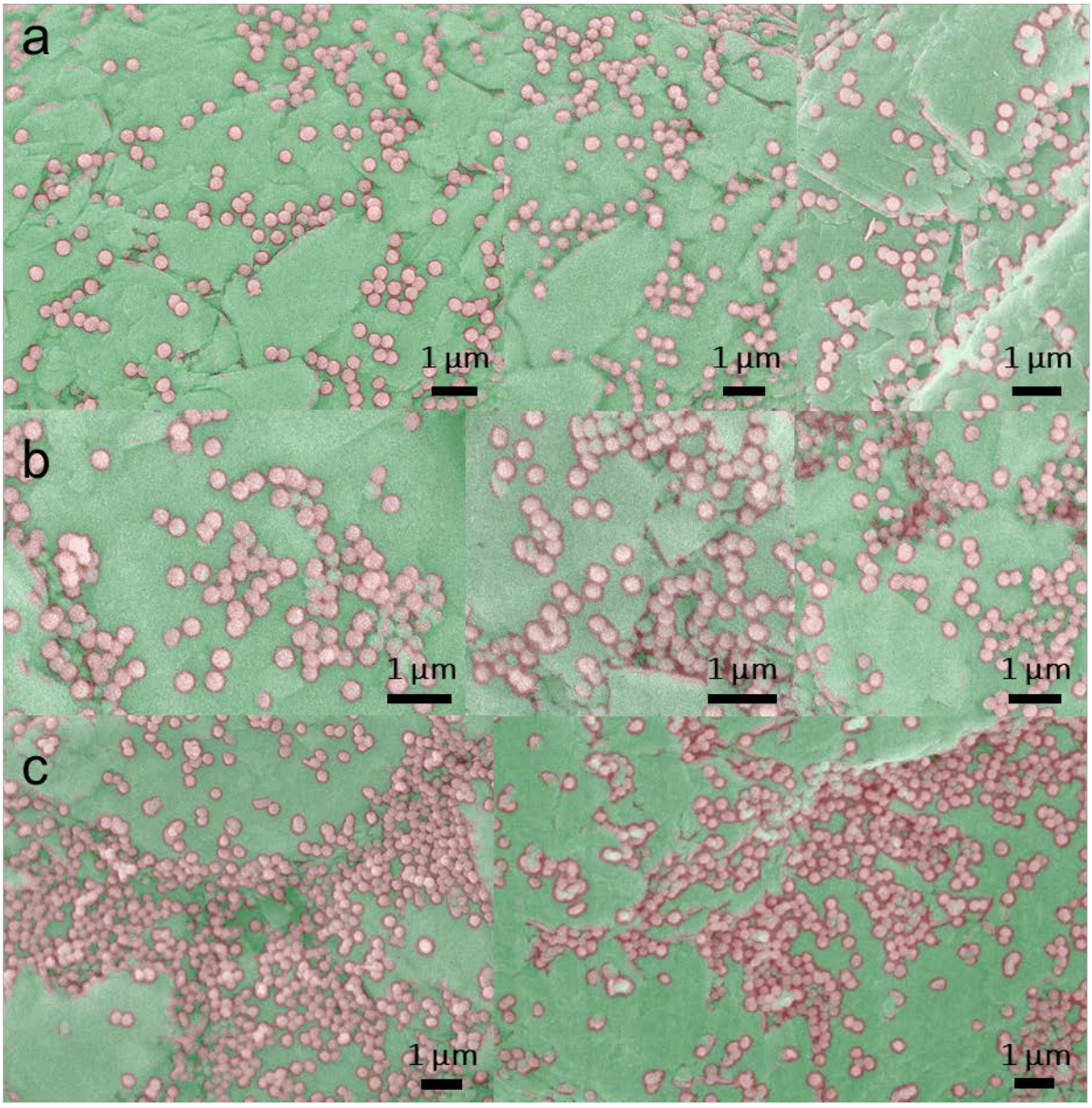


***Figure S2.*** SEM images of PVDF particles, covering graphite surface. The images were superposed with an image generated by a machine learning plugin in ImageJ. This created zones of probability for PVdF particles (in red) and graphite particles (in green). We use these images to estimate the coverage percentage of particles at (a) 1-SM, (b) 3-MM and (c) 15-LM. The software's ability to distinguish and quantify the presence of these particles is a result of the training process, which enhances the accuracy of our analysis.

$$N_{PVdF} = \frac{\mathrm{m} \cdot \chi_{\mathrm{PVdF}}}{\frac{4}{3}\pi\left(\frac{\mathrm{d}_{PVdF}}{2}\right)^3 \cdot \rho_{PVdF}} \qquad N_{Gr} = \frac{m \cdot \chi_{\mathrm{Gr}}}{\frac{4}{3}\pi\left(\frac{[\mathrm{D}\ 4{,}3]_{Gr}}{2}\right)^3 \cdot \rho_{Gr}} \qquad (S1)$$

$$S_{PVdF} = N_{PVDF} \cdot \pi\left(\frac{\mathrm{d}_{PVdF}}{2}\right)^2 \qquad S_{Gr} = N_{Gr} \cdot 4\pi\left(\frac{[\mathrm{D}\ 4{,}3]_{Gr}}{2}\right)^2 \qquad (S2)$$

$$CR_{max} = \frac{S_{PVdF}}{S_{Gr}} = \frac{[\mathrm{D}\ 4{,}3]_{Gr} \cdot \rho_{Gr} \cdot \chi_{\mathrm{PVdF}}}{4 \cdot \mathrm{d}_{PVdF} \cdot \rho_{PVdF} \cdot \chi_{\mathrm{Gr}}} \qquad (S3)$$

$N_{PVdF}$ and $N_{Gr}$ denote the number of PVdF and graphite particles, respectively, present in a mass $m$ of electrode mixture powder. $\chi_{\mathrm{PVdF}}$ and $\rho_{PVdF}$ represent the mass fraction and the density of PVdF, while $\chi_{\mathrm{Gr}}$ and $\rho_{Gr}$ denote those of graphite. $\mathrm{d}_{PVdF}$ represents the diameter of a PVdF particle, determined as the mean value through SEM image analysis. $[\mathrm{D}\ 4{,}3]_{Gr}$ represents the De Brouckere or volume-weighted mean diameter obtained by granulometry.

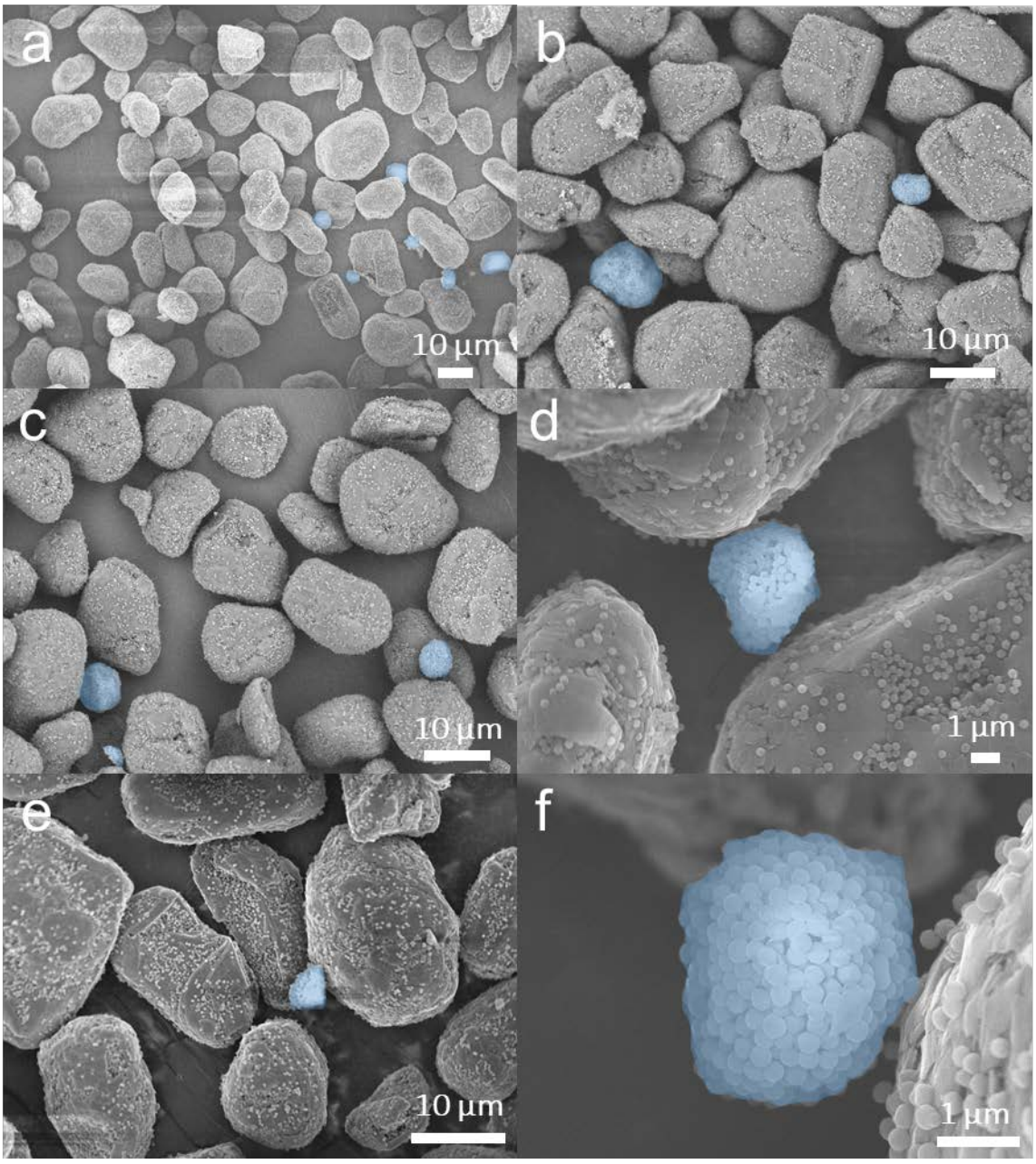


***Figure S3.*** SEM images of electrode powder mixtures. (a,b) corresponds to 1-SM, (c,d) to 3-MM and (e,f) to 15-LM. PVdF agglomerates are slightly highlighted in blue.

$$N_{PVdF\ per\ agglo} = \left(\frac{D_{agglo}}{\mathrm{d}_{PVdF}}\right)^3 \cdot \Phi_{RCP} \qquad N_{agglo} = \frac{N_{PVdF} \cdot \chi_{PVdF,agglo}}{N_{PVdF\ per\ agglo}} \qquad (S4), (S5)$$

**Consolidated electrode**

Morphology and microstructure

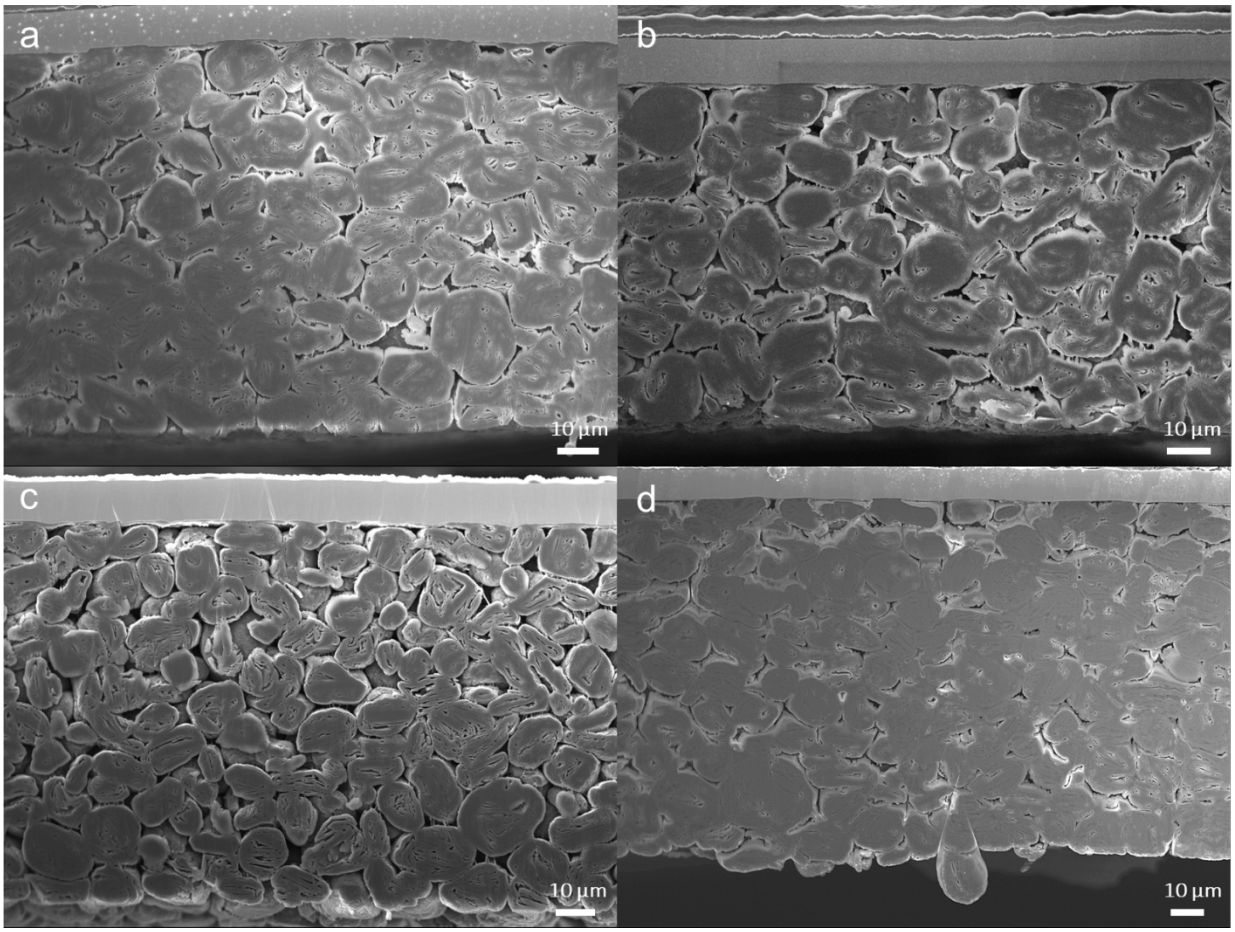


***Figure S4.*** SEM images of electrodes' cross section. (a) 1-DSE, (b) 3-DSE, (c) 15-DSE and (d) WSE.

Mechanical properties

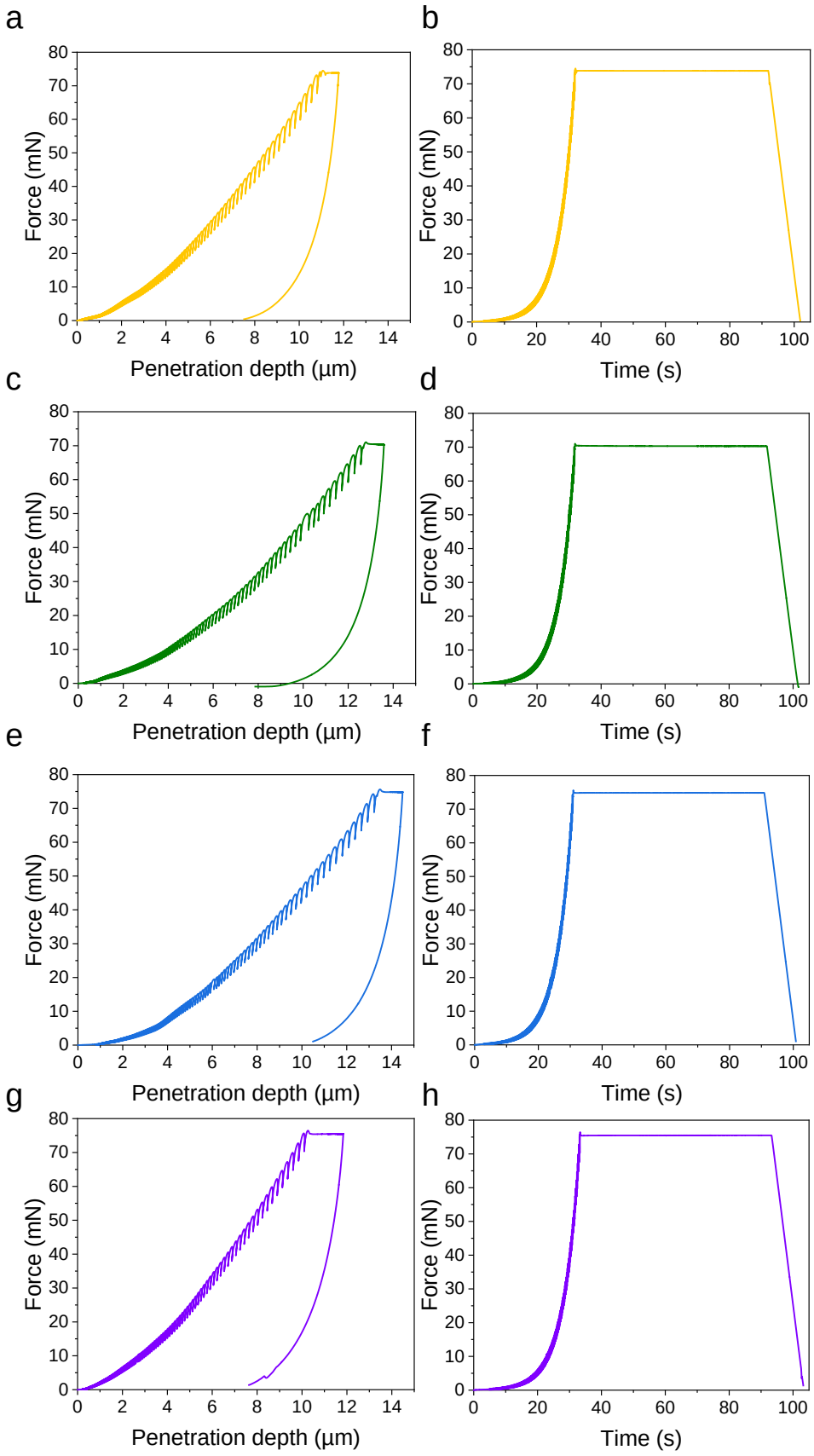


***Figure S5.*** Indentation curves **(**penetration depth vs the load) and load profile for (a-b) 1-DSE, (c-d) 3-DSE, (e-f) 15-DSE, and (g-h) WSE.

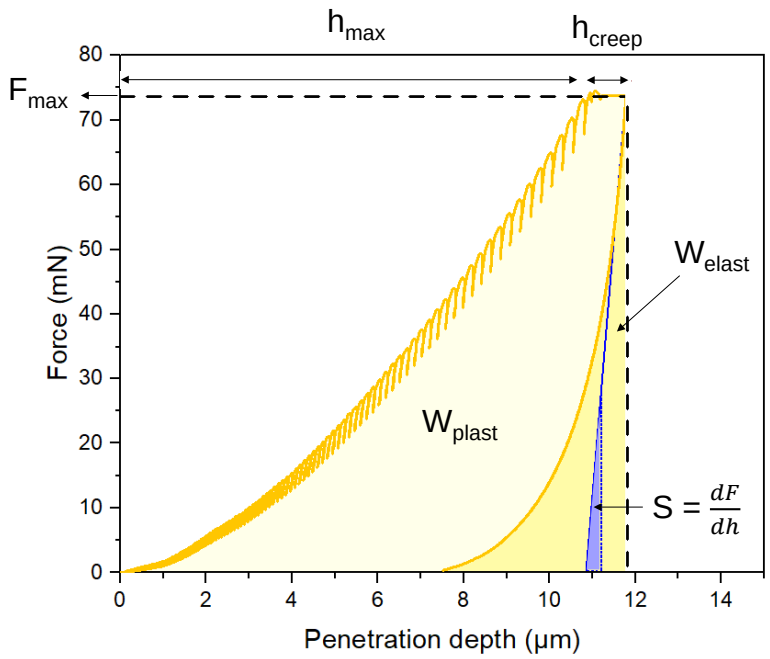


***Figure S6.*** Zoom sur la *Fig. S5a*, highlighting the most significant parameters determined for each of the electrodes. Stiffness of the electrode S is calculated as the derivative of the force with respect to the penetration depth during the unloading part of the curve.

The instrumented hardness (H) (sometimes referred to as ball indentation hardness) and elastic modulus (E) were calculated for each measurement following the equations (S6 to S8):

$$H = \frac{F_{app}}{A_p(h_d)} \qquad E = \frac{(1-\nu^2)}{\frac{1}{E_r} - \frac{(1-\nu_i^2)}{E_i}} \qquad E_r = \frac{\sqrt{\pi}}{\beta}\frac{S}{\sqrt{A_p}} \qquad (S6), (S7), (S8)$$

where $F_{app}$ is the load applied during the set cycle, $A_p(h_d)$ is the projected area that depends on the penetration depth ($h_d$) and on the geometry of the indenter. $E_r$ is the reduced modulus, used to account for the displacement that occurs in both the indenter and the electrode, $E_i$ is the indenter's elastic modulus, $\nu$ and $\nu_i$ are the Poisson ratio of the electrode and the indenter, respectively. $E_r$ is calculated from the stiffness $S$ of the sample (see ***Figure S6***) and $\beta$ is a geometrical factor. The Poisson ratio ($\nu$) for the electrode was fixed at 0.3. Results include values acquired from multiple indentations at different locations (between 5 and 10) resulting in varying maximal penetration depths ($h_{max}$) (between 10 and 15µm) for each (examples for hardness and elastic modulus profiles can be found in ***Figure S7***) for penetration depths between. The creep part of the curve ($h_{creep}$) it is not taken into account for the calculation of neither hardness nor elastic modulus.

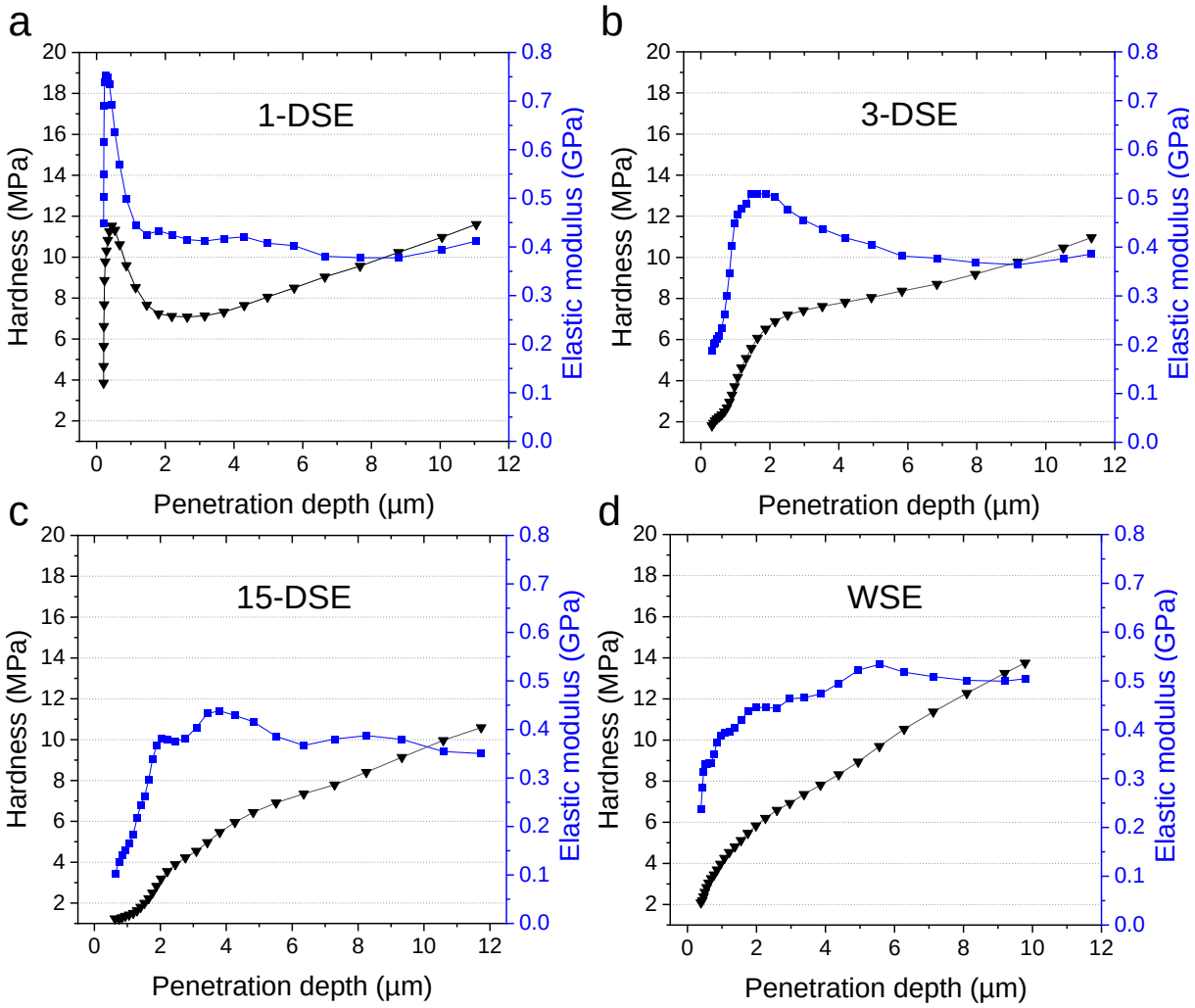


***Figure S7.*** Hardness and elastic modulus indentation profiles (vs penetration depth) examples for (a) 1-DSE, (b) 3-DSE, (c) 15-DSE, and (d) WSE.

The ratio of plastic work to total indentation work applied during loading $W_{total}$ (equal to the sum of $W_{plastic}$ and $W_{elastic}$) can be calculated using the following formula:

$$\eta_{plastic} = \frac{W_{plastic}}{W_{total}} x100 = \frac{W_{plastic}}{W_{plastic} + W_{elastic}} x100 \qquad (S9)$$

Where $W_{plastic}$ is the plastic work, represented as the dissipated work during indentation and $W_{elastic}$ is the rest of work recovered during unloading. Work values are obtained from the displacement curves (***Figure S5***) using the Oliver and Pharr method[1].


***Figure S8.*** Electrode and current collector (CC) interface after peel tests. (a) 1-DSE, (b) 3-DSE and (c) 15-DSE.

Electrochemical properties

**Equations S10-S12.** Porosity determination equations obtained from[2,3].

$$Porosity = \left(1 - \frac{Density_{Real}}{Density_{Theo}}\right) x\ 100 \qquad (S10)$$

Where theoretical and real density are calculated as follows:

$$Density_{Theo} = \frac{1}{\frac{Graphite_{wt\%}}{Graphite_{density}} + \frac{PVDF_{wt\%}}{PVDF_{density}}} \qquad (S11)$$

$$Density_{Real} = \frac{Mass\ loading\ of\ anode}{Thickness\ of\ anode} \qquad (S12)$$

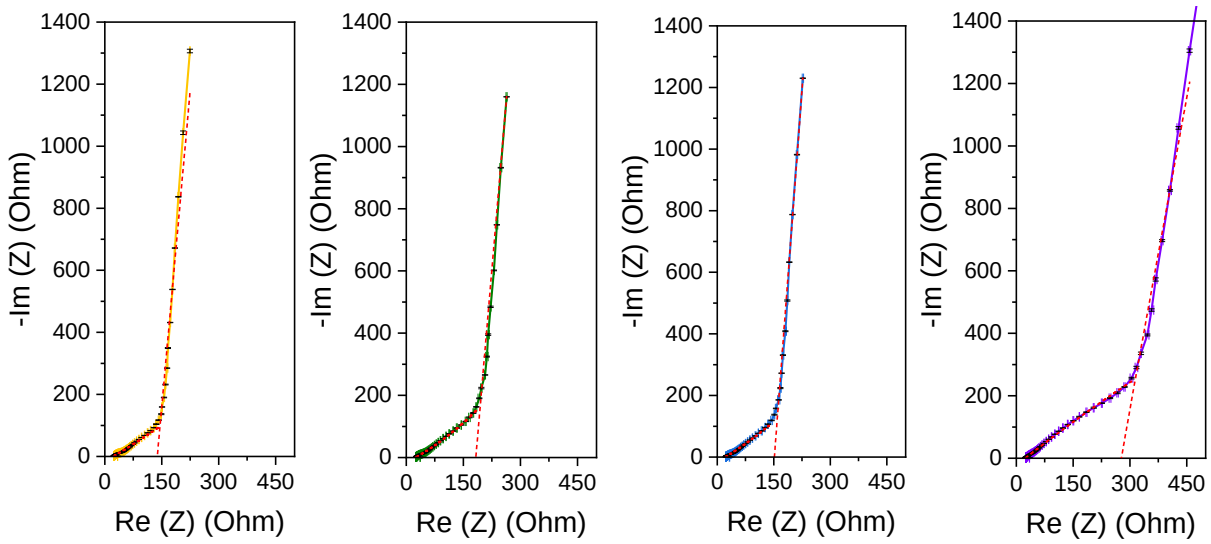


***Figure S9.*** Nyquist impedance plot for (a) 1-DSE, (b) 3-DSE, (c) 15-DSE and (d) WSE.

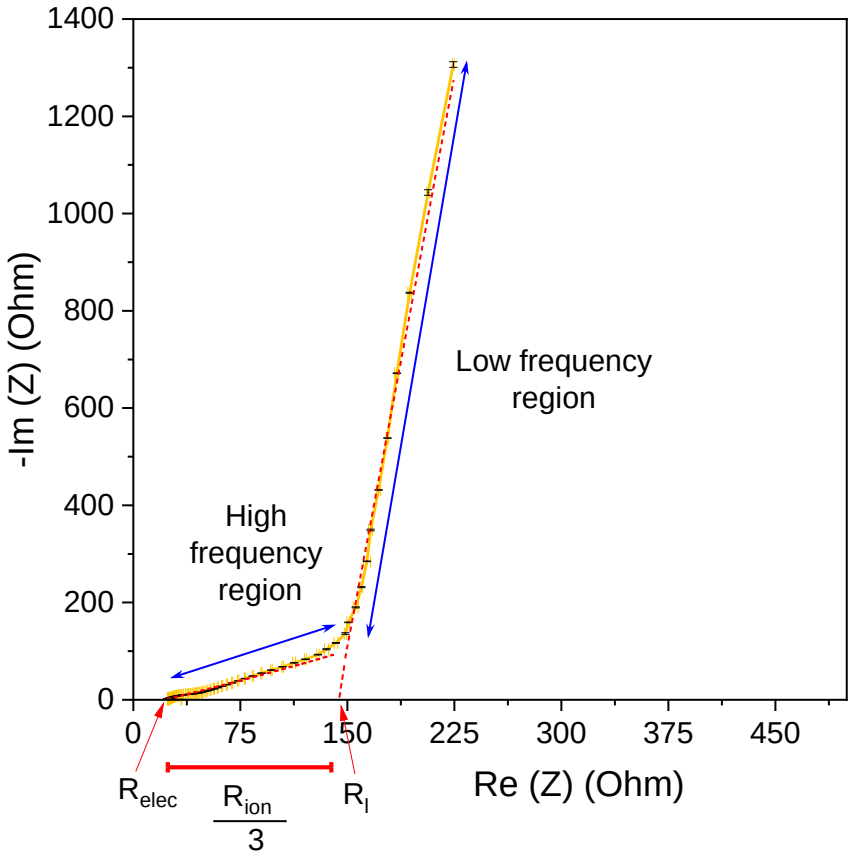


***Figure S10.*** Example of Nyquist impedance plot (for 1-DSE) highlighting the most significant values that we can determine using the blocking-electrolyte method.

According to Landesfeind et al.[4], the ionic resistance ($R_{ion}$) can be roughly estimated by extrapolating the low-frequency region or linear portion of the curve ($R_l$) and determining the intercept of the high-frequency region ($R_{elec}$). The difference between $R_l$ and $R_{elec}$ is approximately equal to $R_{ion}/3$. The intrinsec ionic conductivity of the electrolyte ($\kappa$) can be approximated by using the TLM with blocking conditions (Eq. 2) using the $R_{elec}$ values for each of the electrodes. Celgard 2400 fabricator reported a thickness of 25 µm and a porosity of 41%. The tortuosity factor was determined by Thorat et al. to be 3.15.[5]. The obtained $\kappa$ value was around 0.48 $mS \cdot cm^{-1}$, which falls within the range of values obtained in other studies.[4,6,7]

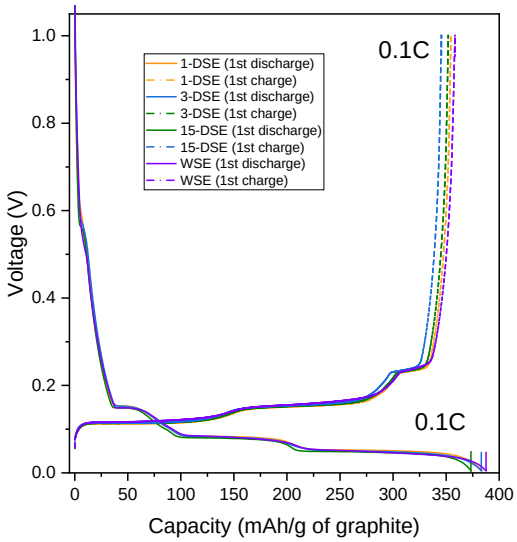


***Figure S11.*** (a) First dicharge-charge capacities for electrodes at 0.1C.

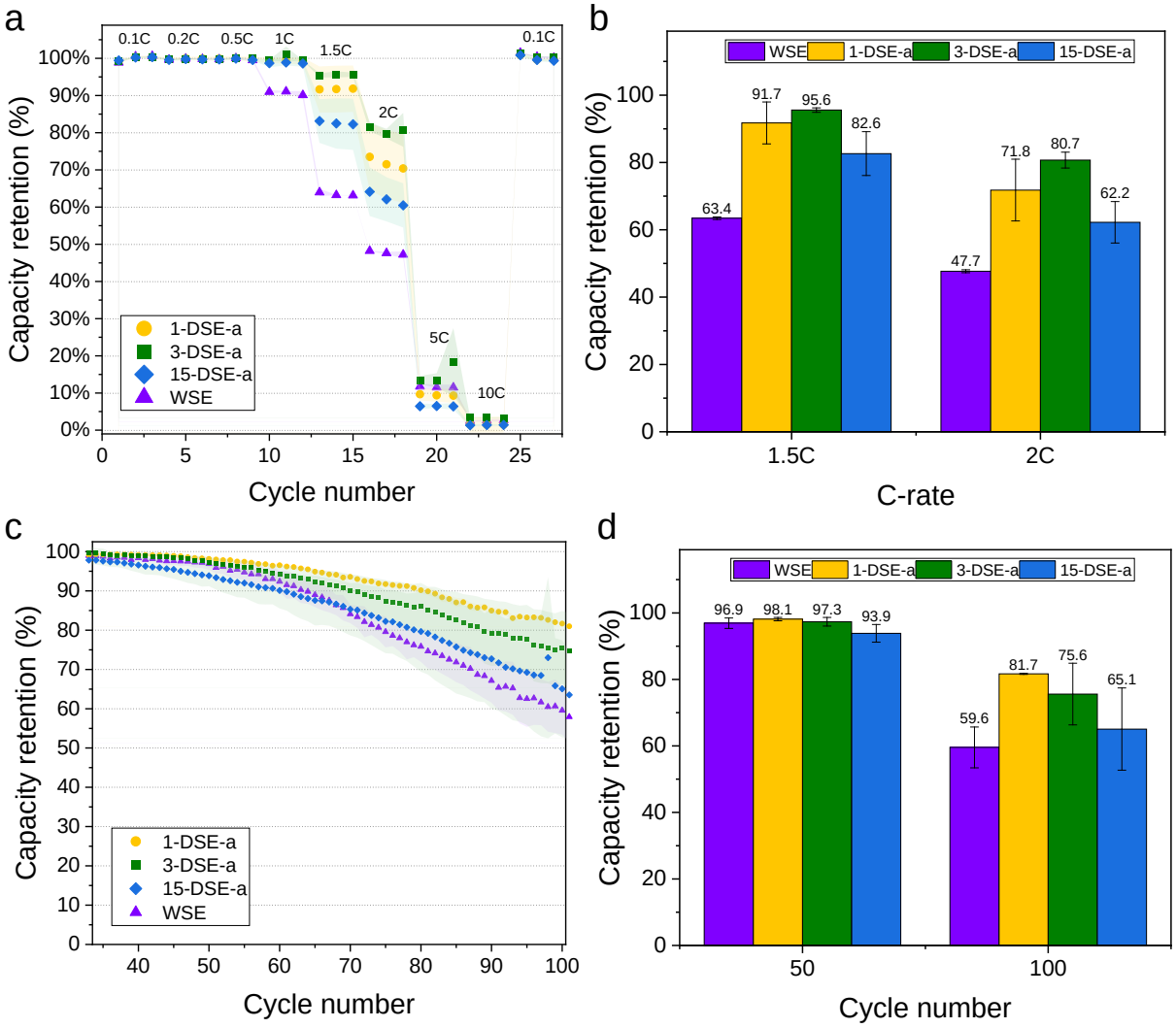


***Figure S12.*** Half-cell in coin cell format: (a) Rate capability evaluation and (b) focus on capacity retention at 1.5C and 2C. (c) Long-term cycling capacity retention at a lithiation/delithiation C-rate of 0.2C and (d) focus on capacity retention at the 50$^{th}$ and 100$^{th}$ cycles.

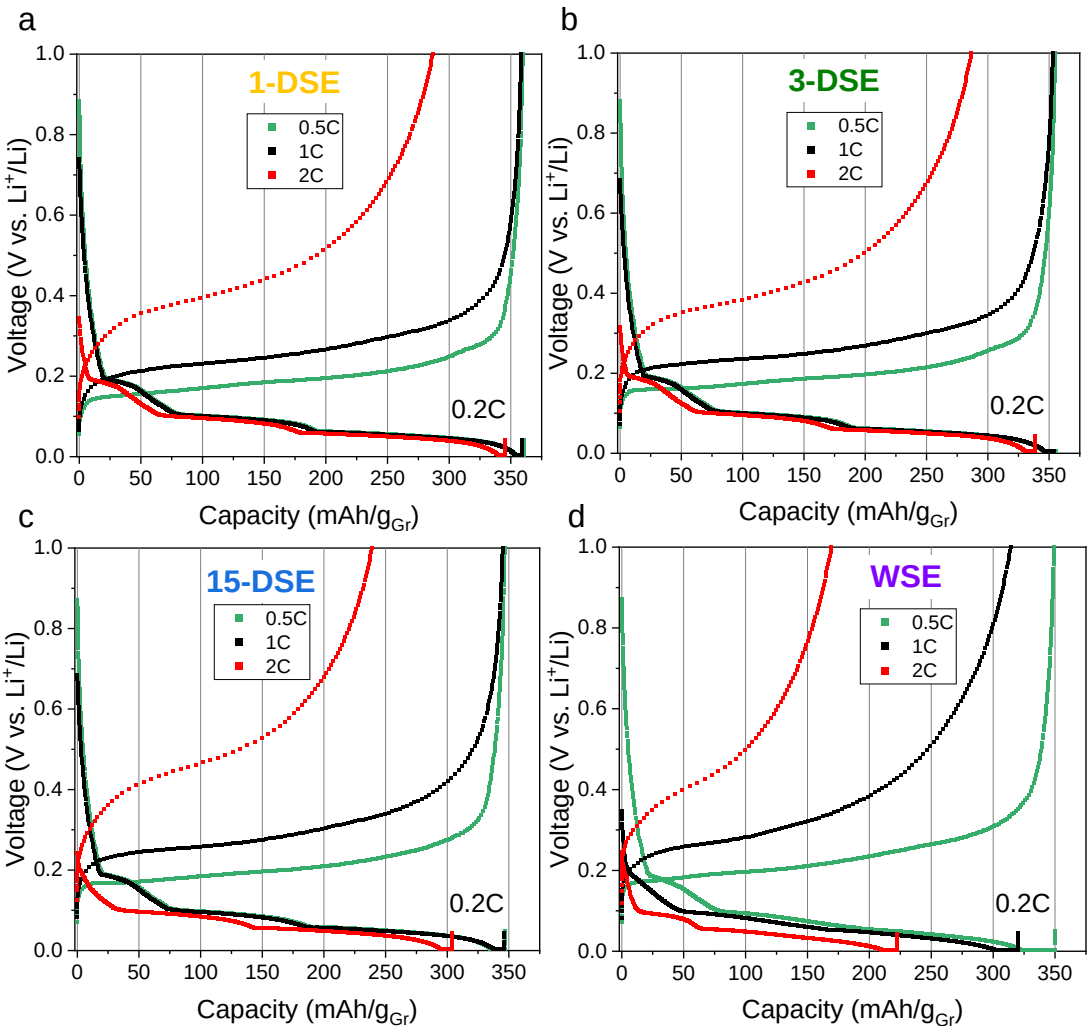


***Figure S13.*** (a-d) voltage (V vs $Li^+/Li$) vs. capacity (mAh/g of graphite) profiles for electrodes at three different C-rate (0.5C, 1C and 2C) in delithiation.

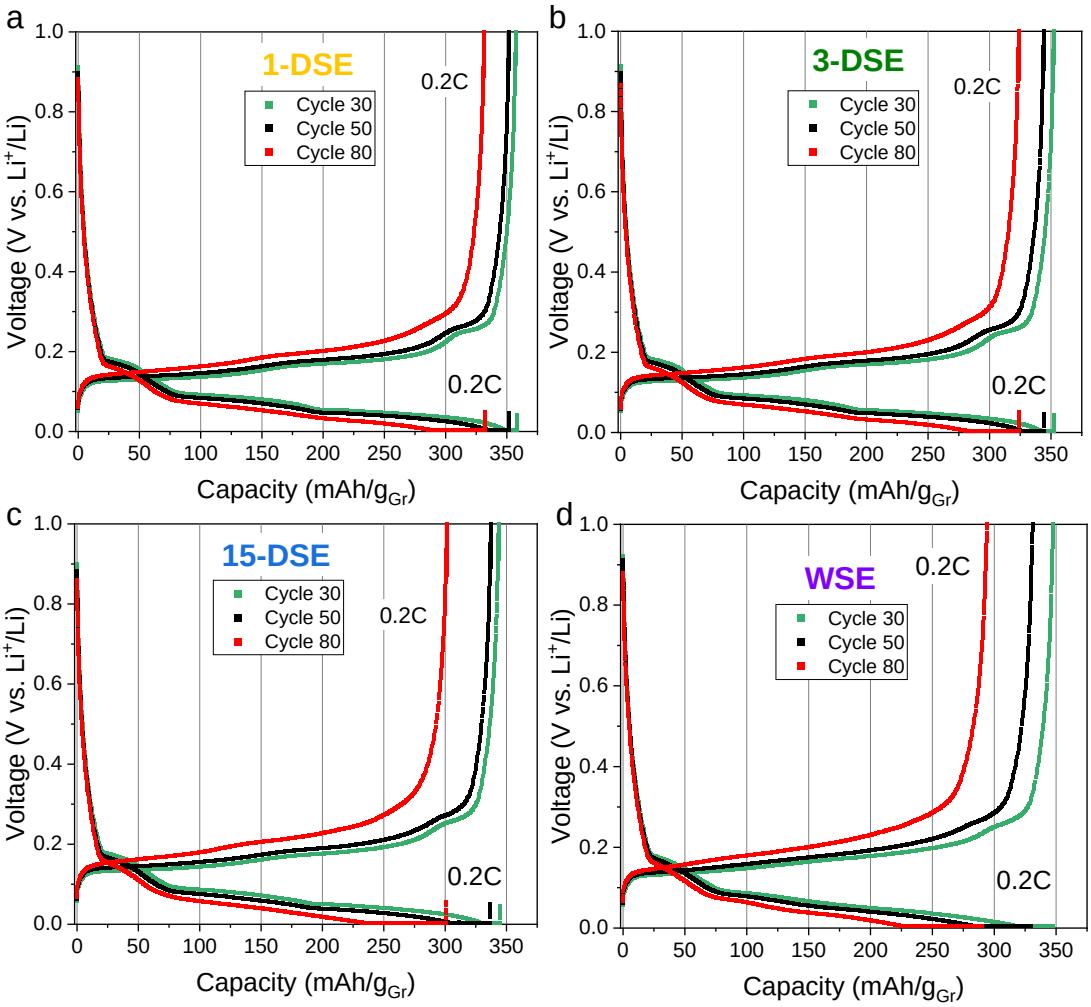


***Figure S14.*** (a-d) voltage (V vs $Li^+/Li$) vs. capacity (mAh/g of graphite) profiles for the electrodes at $30^{th}$, $50^{th}$ and $80^{th}$ cycles (0.2C rate).

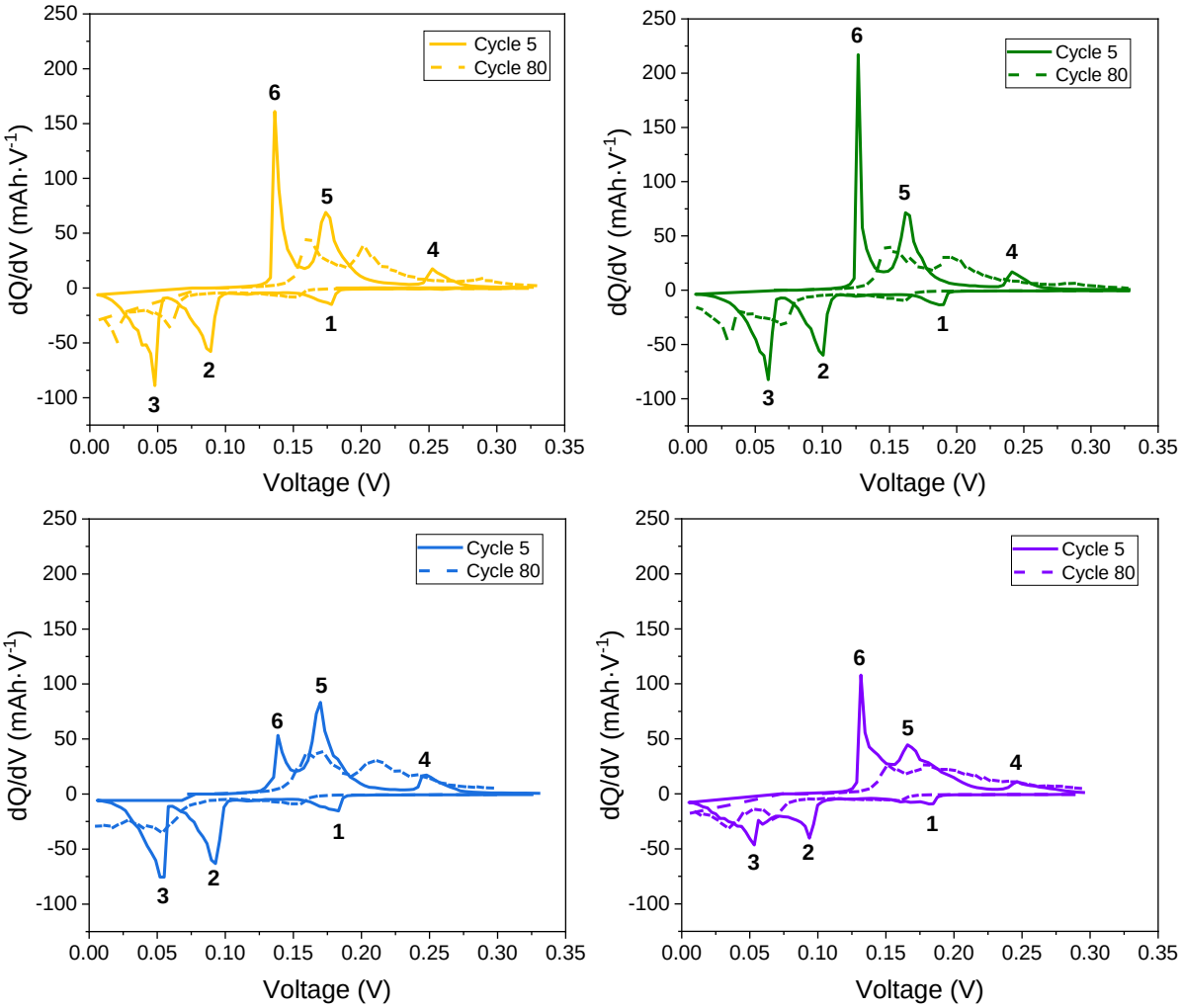


***Figure S15.*** Incremental capacity (dQ/dV) vs voltage (V) plots for (a) 1-DSE, (b) 3-DSE, (c) 15-DSE, (d) WSE at cycles 5 and 80 (C-rate of 0.2C). The dQ/dV peaks position is noted with the numbers 1-6.

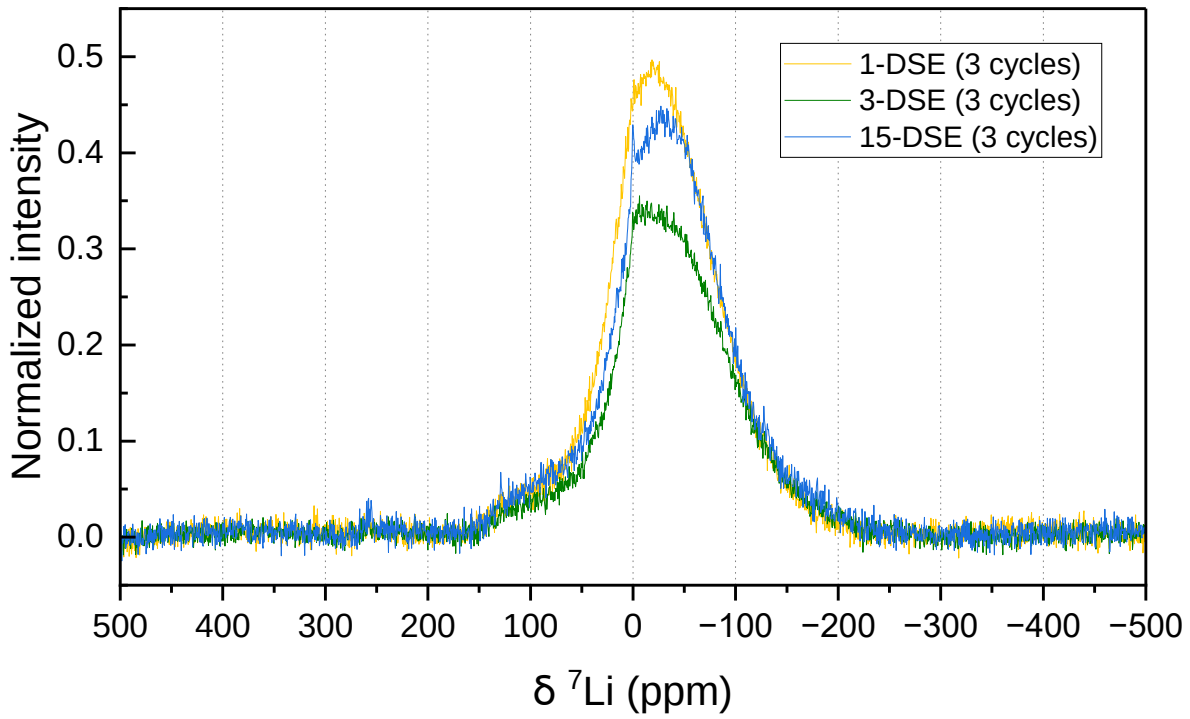


***Figure S16.*** Solid-state $^{7}$Li MAS-NMR spectra for 1-DSE, 3-DSE and 15-DSE performed after the first 3 formation cycles.

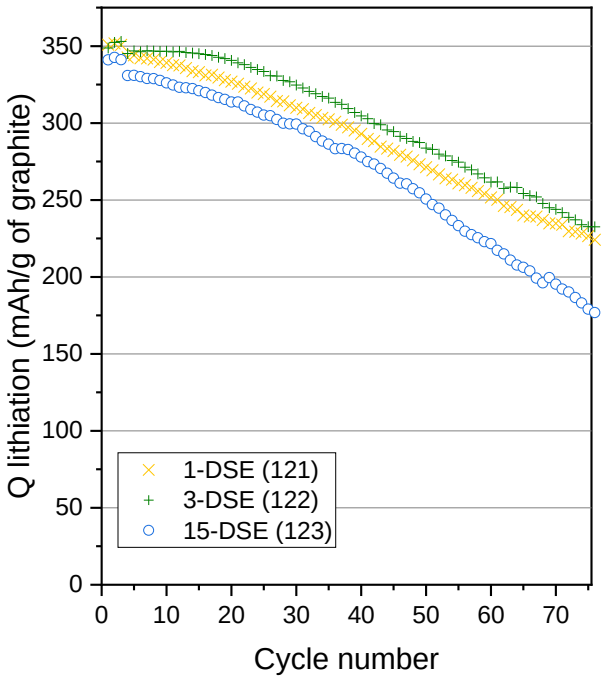


***Figure S17.*** Long-term cycling of half-cells at a discharge/charge C-rate of 0.1.C for the first three cycles and then 0.2C prepared for mechanical and electrical testing.

## References


(1) Oliver, W. C.; Pharr, G. M. An Improved Technique for Determining Hardness and Elastic Modulus Using Load and Displacement Sensing Indentation Experiments. *J. Mater. Res.* **1992**, *7* (6), 1564–1583. https://doi.org/10.1557/JMR.1992.1564.

(2) Marks, T.; Trussler, S.; Smith, A. J.; Xiong, D.; Dahn, J. R. A Guide to Li-Ion Coin-Cell Electrode Making for Academic Researchers. *J. Electrochem. Soc.* **2011**, *158* (1), A51. https://doi.org/10.1149/1.3515072.

(3) Wang, M.; Hu, J.; Wang, Y.; Cheng, Y.-T. The Influence of Polyvinylidene Fluoride (PVDF) Binder Properties on $LiNi_{0.33}Co_{0.33}Mn_{0.33}O_2$ (NMC) Electrodes Made by a Dry-Powder-Coating Process. *J. Electrochem. Soc.* **2019**, *166* (10), A2151–A2157. https://doi.org/10.1149/2.1171910jes.

(4) Landesfeind, J.; Hattendorff, J.; Ehrl, A.; Wall, W. A.; Gasteiger, H. A. Tortuosity Determination of Battery Electrodes and Separators by Impedance Spectroscopy. *J. Electrochem. Soc.* **2016**, *163* (7), A1373–A1387. https://doi.org/10.1149/2.1141607jes.

(5) Thorat, I. V.; Stephenson, D. E.; Zacharias, N. A.; Zaghib, K.; Harb, J. N.; Wheeler, D. R. Quantifying Tortuosity in Porous Li-Ion Battery Materials. *Journal of Power Sources* **2009**, *188* (2), 592–600. https://doi.org/10.1016/j.jpowsour.2008.12.032.

(6) Landesfeind, J.; Eldiven, A.; Gasteiger, H. A. Influence of the Binder on Lithium Ion Battery Electrode Tortuosity and Performance. *J. Electrochem. Soc.* **2018**, *165* (5), A1122–A1128. https://doi.org/10.1149/2.0971805jes.

(7) Pouraghajan, F.; Knight, H.; Wray, M.; Mazzeo, B.; Subbaraman, R.; Christensen, J.; Wheeler, D. Quantifying Tortuosity of Porous Li-Ion Battery Electrodes: Comparing Polarization-Interrupt and Blocking-Electrolyte Methods. *J. Electrochem. Soc.* **2018**, *165* (11), A2644–A2653. https://doi.org/10.1149/2.0611811jes.